

1 **Internal tides in the Solomon Sea in contrasted ENSO conditions**

2
3 Michel Tchilibou¹, Lionel Gourdeau¹, Florent Lyard¹, Rosemary Morrow¹, Ariane Koch
4 Larrouy¹, Damien Allain¹, Bughsin Djath²
5
6
7
8

9 1) Laboratoire d'Etude en Géophysique et Océanographie Spatiales (LEGOS), Université de
10 Toulouse, CNES, CNRS, IRD, UPS, Toulouse, France
11

12 2) Helmholtz-Zentrum Geesthacht Max-Planck-Strase, Geesthacht, Germany,
13
14
15
16
17

18 **Contact:**

19 Michel Tchilibou: michel.tchilibou@legos.obs-mip.fr

20 Lionel Gourdeau: lionel.gourdeau@legos.obs-mip.fr

21 Florent Lyard: florent.lyard@legos.obs-mip.fr

22 Rosemary Morrow: rosemary.morrow@legos.obs-mip.

23 Ariane KochLarrouy: Ariane.Koch-Larrouy@legos.obs-mip.fr

24 Damien Allain: Damien.allain@legos.obs-mip.fr

25 Bughsin Djath: bughsin.djath@hzg.de
26
27

28 **Abstract**

29
30 Intense equatorward western boundary currents transit the Solomon Sea, where active
31 mesoscale structures exist with energetic internal tides. In this marginal sea, the mixing induced
32 by these features can play a role in the observed water mass transformation. The objective of
33 this paper is to document the M2 internal tides in the Solomon Sea and their impacts on the
34 circulation and water masses, based on two regional simulations with and without tides. Since
35 the Solomon Sea is under the influence of ENSO, the characteristics of the internal tides are also
36 analyzed for two contrasted conditions: the January-March 1998 El Niño and the April-June 1999
37 La Niña. The generation, propagation and dissipation of the internal tides are sensitive to
38 changes in stratification and mesoscale activity, and these differ between these contrasted El
39 Niño and La Niña case studies. Mode 1 is the dominant vertical mode to propagate baroclinic
40 tidal energy within the Solomon Sea, but Mode 2 becomes more energetic during the El Niño
41 period when the stratification is closer to the surface. The La Niña period with a higher level of
42 mesoscale activity exhibits more incoherent internal tides. These results illustrate the complexity
43 of predicting internal tides in marginal seas in order to clearly observe meso and submesoscale
44 signatures from altimetric missions, including the future SWOT mission. Diapycnal mixing
45 induced by tides contributes to a stronger erosion of the salinity maximum of the upper
46 thermocline water, and to cooling of the surface temperature interacting with the atmosphere.
47 Such effects are particularly visible in quieter regions, where particles may experience the tidal
48 effects over a longer time. However, when averaged over the Solomon Sea, the tidal effect on
49 water mass transformation is an order of magnitude less than that observed at the entrance and
50 exits of the Solomon Sea. These localized sites appear crucial for diapycnal mixing, since most of
51 the baroclinic tidal energy is generated and dissipated locally here, and the different currents
52 entering/exiting the Solomon Sea merge and mix. Finally, the extreme ENSO condition case
53 studies suggest the strong role of local circulation changes as well as stratification changes, in
54 modifying the internal tides.

55
56 **1. Introduction**

57
58 The Solomon Sea is a marginal sea that is the last passageway for the low-latitude western
59 boundary currents (LLWBCs) of the Southwest Pacific that connect the subtropics to the equator,
60 and supply water of subtropical origin to the Equatorial Undercurrent (EUC), Warm Pool, and
61 Indonesian Throughflow (Tsushiya, 1989; Grenier et al., 2011). It is an important place for
62 tropical circulation and climate that motivates the CLIVAR Southwest Pacific Ocean Circulation and
63 Climate Experiment (SPICE) program (Ganachaud et al., 2014). Marginal seas have long been
64 identified as regions that contribute significantly to kinetic energy dissipation and water mass
65 modification (Munk and Wunsch, 1998; Price and Yang, 1998; Egbert and Ray, 2000). Their
66 topographic properties make them unique regions where water properties are transformed by lateral
67 stirring and vertical mixing due to the energetic eddy field and the tidal-driven internal wave field.
68 An abundant literature exists on the South China Sea and the Indonesian Seas, illustrating this
69 distinctive feature of marginal seas, but not in the Solomon Sea, even though the Southwest Pacific
70 and in particular the Solomon Archipelago are recognized as generation areas of energetic
71 internal tides (Niwa and Hibiwa, 2001). Internal tides with phase locked solitary waves have
72 been observed during the COARE experiment, and they appear to propagate
73 northeastward from the Solomon Islands (Pinkel, 1997; Gourdeau et al., 1998).

74
75 The Solomon Sea is bordered by the main island of Papua New Guinea (PNG) to the West, the
76 PNG islands of New Britain (NB) and New Ireland (NI) to the North, and the Solomon Islands to
77 the East (Fig.1). The circulation in this semi enclosed basin is highly constrained by such
78 bathymetric features, and has been described in numerous recent studies, from observations
79 (Cravatte et al., 2011; Hristova and Kessler, 2012; Kessler et al., 2019; Davis et al., 2012; Gasparin

30 et al., 2012), and model outputs (Melet et al., 2010; Djath et al., 2014). A strong Low Latitude
31 Boundary Current (LLWBC), the New Guinea Coastal Undercurrent (NGCU) fed by the Gulf of
32 Papua Current (GPC) and the North Vanuatu Jet (NVJ), flows from the southern entrance of the
33 Solomon Sea along the PNG coast. When approaching the New Britain coast, it separates into
34 two branches that exit the Solomon Sea through Vitiaz and Solomon Straits. The NGCU flows at
35 the thermocline level below highly variable surface currents including the New Guinea Coastal
36 Current (NGCC), and the Solomon Strait Inflow (SSI) that is a branch of the South Equatorial
37 Current (SEC) that enters the Solomon Sea through the Solomon Strait. Instabilities of these
38 large-scale currents generate large mesoscale eddies that account for most of the surface eddy
39 kinetic energy (EKE) (Gourdeau et al, 2014, 2017; Hristova et al. (2014), and interaction of the
40 mesoscale flow with topographic features generate submesoscale eddies and fronts (Srinivasan
41 et al., 2017).

42
43 Specific water masses entering the Solomon Sea are the South Pacific tropical Water (SPTW, $\sigma_\theta \sim$
44 24.5 kg m^{-3}) in the upper thermocline level (UTW, $23.3 < \sigma_\theta < 25.7 \text{ kg m}^{-3}$), referred to as the upper
45 salinity maximum water, and the Antarctic Intermediate Water (AAIW, $\sigma_\theta \sim 27.2 \text{ kg m}^{-3}$) in the
46 intermediate water range (IW, $26.7 < \sigma_\theta < 27.5$) identified by a salinity minimum. These water
47 masses undergo significant modification that erodes their extrema along their pathways through
48 the Solomon Sea. This is characterized by a cooling and freshening of the SPTW, and a warming
49 and increased salinity of the AAIW, mainly due to diapycnal mixing (Fig. 3 in Gernineaud et al.,
50 2016; Melet et al., 2011). The modification of UTW affects the western Pacific with potential
51 downstream effects on the eastern Pacific when the EUC upwells in the tropical eastern Pacific
52 Ocean (Tsuchiya et al., 1989; Fine et al., 1994; Grenier et al., 2011; Qin et al., 2016).

53
54 In the Solomon Sea, Thorpe scales and finescale turbulence methods were applied to in situ
55 observations to indirectly estimate the rate of dissipation of kinetic energy (Alberty et al., 2017).
56 Depth-mean energy dissipation in the Solomon Sea is elevated by a factor of eight relative to the
57 rest of the equatorial Pacific, and energy dissipation is maximum in the surface and thermocline
58 layers ($4.1\text{--}23 \text{ } 10^{-8} \text{ W kg}^{-1}$). To model this increased water mass mixing correctly in the Solomon
59 Sea, tidal effects need to be included. Melet et al. (2011) used the tide based vertical diffusivity
60 parameterization proposed by Koch-Larrouy et al. (2007) for the Indonesian Seas. This
61 parameterization is based on the assumptions that all of the energy of the internal tides within a
62 marginal sea is dissipated within that sea, and that energy dissipation is assumed to be maximum
63 in the thermocline. Their modeled salinity without this tidal parameterization is biased high over
64 the $24.5\text{--}27.5 \text{ } \sigma_\theta$ range compared to observed properties, although it remains biased low with
65 the parameterization, such that the erosion of SPTW is too strong.

66
67 This tidal parameterization is applied over the entire marginal sea, and aims to take into account
68 the general effects of internal tides in an ocean model. Yet internal tides are generated at a few
69 specific locations where strong tidal currents encounter sharp topography in a stratified ocean. A
70 global view of their generation, propagation, and dissipation has emerged from satellite
71 altimetry observations (Ray and Mitchum, 1997; Ray and Zaron, 2016; Zhao et al., 2018) and
72 global high-resolution numerical models (Arbic et al., 2010; Shriver et al., 2012; Simmons et al.,
73 2004, Niwa and Hibiwa, 2014). Several studies have focused on the low vertical modes. M2
74 internal tides in the Pacific Ocean have been particularly investigated because of the numerous
75 archipelagoes that are sources of internal tide generation. Regional studies based on in-
76 situ/satellite data and regional models have documented internal tides at the Hawaiian ridge
77 (Merrifield and Holloway, 2002; Nash et al., 2006; Chavanne et al., 2010; Zhao et al., 2010), and
78 at the Indonesian archipelago (Robertson and Field, 2008; Nagai and Hibiya, 2015; Nughoru et
79 al., 2017). As far as we know, no dedicated studies have focused on internal tides in the South
80 West tropical Pacific, despite the high semi diurnal baroclinic tidal energy found here (Niwa and
81 Hibiwa, 2011; Shriver et al., 2012). The main motivation of this paper is to document internal

32 tides at the Solomon archipelago and their effects on the circulation and water masses in the
33 Solomon Sea based on a regional model with and without tidal forcing.

34
35 Satellite altimeter maps show low mode phase-locked internal tides propagating across basins
36 for thousands of kilometers (Shriver et al., 2012, Zhao et al., 2016, Ray and Zaron, 2016). This
37 picture of coherent, phase-locked internal tides is somewhat partial as shown recently by several
38 authors that point to the importance of non-stationary tides (Zaron, 2017; Shriver et al., 2014;
39 Buijsman et al., 2017). In the world oceans, up to 44% of the total semidiurnal internal tide signal
40 is incoherent, and in the equatorial Pacific most of the tidal motions are incoherent (Buijsman et
41 al., 2017). Several mechanisms contribute to the incoherence of internal tides. First, the internal
42 tide generation may vary in time due to local changes in stratification (Colosi and Munk, 2006;
43 Chavanne et al., 2010). Second, the propagation of the low-mode internal tides is modulated by
44 spatial and temporal variability in stratification, currents, and vorticity with detectable changes
45 in tidal SSH (Zilberman et al., 2011; Ponte and Klein, 2015).

46
47 The South West Tropical Pacific is also marked by large interannual variability associated with the
48 El Niño Southern Oscillation (ENSO) with LLWBCs that vary to counterbalance interannual
49 changes in the interior geostrophic flow (Melet et al., 2010b, 2013, Histrova and Kessler, 2012).
50 The Solomon Sea experiences strong interannual variations in relation to ENSO. These include
51 asymmetric circulation differences between El Niño and La Niña conditions that greatly impact
52 on the mesoscale activity, and large temperature and salinity modifications particularly notable
53 for the thermocline waters (Melet et al., 2013). So, it is suspected that internal tides in the
54 Solomon Sea could be modulated by extreme ENSO conditions, with possible consequences on
55 mixing of water masses flowing through to the equator.

56
57 This particular study is a first attempt to investigate and describe internal tides over the complex
58 Solomon Sea and their interaction with the mesoscale circulation, as well as to investigate their
59 potential role on water mass transformation. We will address this issue using regional
60 simulations at high resolution ($1/36^\circ$), with and without tidal forcing, that have been performed
61 during a 3 year period. We will also consider case studies for two extreme periods: the January-
62 March (JFM) 1998 El Niño and the April-June (AMJ) 1999 La Niña that exhibits different
63 stratification and mesoscale activity.

64
65 The paper is organized as follows. Section 2 describes the regional model of the Solomon Sea
66 with and without tides and the methodology used to analyse the tides. Section 3 describes the
67 contrasted fields between the 1998 El Niño and the 1999 La Niña events for the different
68 simulations. Section 4 describes the generation, propagation and dissipation of the M2 baroclinic
69 tide during the two ENSO conditions with a focus on their vertical signatures. Section 5 describes
70 water mass transformation due to the tides over the longer 3-year period of the simulations. We
71 illustrate some changes in the surface layer water mass properties due to tides for the
72 contrasted ENSO conditions. Discussion and conclusion are given in section 6.

73 74 **2. Data and method**

75 76 **2.1 Model description : NEMO**

77
78 The numerical model of the Solomon Sea used in this study is based on the Nucleus for European
79 Modelling of the Ocean (NEMO) code (Madec, 2008) that resolved the standard primitive
80 equations. It is a $1/36^\circ$ horizontal resolution model originally developed by Djath et al. (2014)
81 that encompasses the Solomon Sea from 143°E to 165.5°E in longitude and from 13°S to 2°S in
82 latitude. Atmospheric boundary conditions are diagnosed through classical bulk formulae (Large
83 and Yeager, 2009), and wind, atmospheric temperature and humidity are provided from the 3-

hourly ERA-Interim reanalysis (Dee et al., 2011). This 1/36° resolution model is embedded into a global NEMO 1/12° ocean model forced with similar atmospheric boundary conditions, and one-way controlled using an open boundary strategy (Treguier et al., 2001). The version used here is discretized on the vertical with 75 levels, and includes the option of realistic tidal forcing. The simulation with tides is forced at the open boundary by prescribing the first nine main tidal harmonics (M2, S2, N2, K2, K1, O1, P1, Q1, M4) as defined from the global tidal atlas FES2014 (Carrere et al., 2018) through a forced gravity wave radiation condition. More technical details on this configuration may be found in Tchilibou et al. (2018).

Two simulations are performed: one without tidal forcing (R36), and one with tidal forcing (R36T) over the 3-year 1997–1999 period. Daily mean model outputs are saved as R36(T)d. Instantaneous fields are saved hourly (R36(T)h) to document the baroclinic tides during the two contrasting 3-month periods: from January–March 1998, and from April–June 1999. The former period corresponds with summer austral conditions during an El Niño period, and the latter with fall austral conditions during a La Niña period. For these two periods the interannual conditions dominate the effect of the mean seasonal cycle (not shown). These two periods in R36Th offer extremes in local stratification conditions, with a possible impact on the internal tides. The longer series of R36d and R36Td will be useful to investigate the effects of high frequency baroclinic tides on the Solomon Sea water masses.

Very few in situ data exist to validate the high frequency signal from the model. Some comparisons with coastal tide gauges and a mooring in Solomon Strait present satisfactory results at very localised positions (Tchilibou, 2018). The spatial patterns of phase-locked internal tide SSH patterns from 20 years of satellite altimetry will be compared with the R36Th 3-month model patterns under contrasted ENSO conditions in section 4.2. Tchilibou et al. (2018) also used these simulations in the western Pacific, with and without tides, to illustrate how internal tides can explain the discrepancy in sea surface height wavenumber spectra, apparent in models (without tides) and altimetric data.

2.2 CARS climatology

CARS is a global ocean climatology on a ½ degree grid of seasonal ocean water properties delivered by CSIRO (www.cmar.csiro.au/cars). CARS differs from other climatologies as it employs extra in-house quality control of input data, and the mapping algorithm uses an adaptive-length scale loess filter to maximize resolution in data-rich regions, and takes into account topographic barriers. The result is an improved definition of oceanic structures and more accurate point values (Dunn and Ridgway, 2002). The CARS climatology will be used to provide some model validation, given the short period of the simulation including two extreme events.

2.3 Tidal decomposition and energetics

a) Barotropic/baroclinic tides decomposition

The central issue is to perform an accurate separation of the barotropic and baroclinic tide components, in terms of velocity and pressure as discussed in Nugroho et al. (2017). Although intuitive, this issue is not trivial and we need to define precisely the meaning of “barotropic” and “baroclinic” dynamical terms. The method used to separate surface and internal tides ultimately defines properties such as internal tide generation and the depth structure of the internal tide energy flux (Kelly et al., 2010).

The most common definitions can be summarized as follow:

35 1, barotropic tides are the ones that would be present in the absence of ocean stratification
36 (uniform density ocean), and baroclinic tides are the departure from those barotropic tides when
37 stratification is taken into account. This definition has been widely adopted by many authors.
38 However, barotropic tides in a non-stratified ocean will differ significantly from barotropic tides
39 in a stratified ocean. As a consequence, the “baroclinic” tides obtained by differencing non-
40 stratified ocean tides and stratified ocean tides will contain parasite barotropic residuals.

41
42 2, barotropic tides are the depth-averaged part of the tidal dynamics in a stratified ocean,
43 baroclinic tides then being the residual between the full 3D tides and the barotropic tides. This
44 definition is quite conventional and popular, and mostly acceptable for first order analysis. This
45 reflects the idea that baroclinic quantities vanish when integrated with depth (also called the
46 baroclinicity condition). This method has some consistency with model modes under a rigid lid
47 assumption, but in the free surface case, it doesn’t take account of the surface pressure, leading
48 to an unsatisfactory tidal energy budget. The surface tide pressure can be expressed as the depth
49 average of total pressure plus an additional depth-dependent profile of pressure, which is due to
50 isopycnal heaving by free surface movements (Kelly et al., 2010).

51
52 3, barotropic tides are the fast mode in a Sturm-Liouville vertical mode theoretical framework,
53 and baroclinic tides are the slow modes. By using modal decomposition, this technique solves
54 the inconsistencies that come from surface pressure variations due to isopycnal displacement.
55 When this decomposition is applied on idealized cases, it also gives a barotropic energy flux that
56 is consistent with energy conversion, and has a good agreement with observations (Kelly, 2012).
57 This definition has a much better physical meaning, and has attracted much attention in the tidal
58 community. It has been applied on models with realistic forcing and complex bottom topography
59 such as in the Indonesian Seas (e.g., Nugroho et al., 2017).

50
51 In this study, we will use the vertical mode decomposition (3) to define and separate the
52 barotropic and baroclinic tides. In practice, the vertical mode computation and the simulation’s
53 decomposition have been performed by solving the generalized Sturm-Liouville
54 eigenvector/eigenvalue problem. Each successive mode decreases in group speed and increases
55 in horizontal wavenumber. The lowest-mode tide ($n = 0$) is the surface barotropic tide, and the
56 higher-mode tides ($n \geq 1$) make up the internal tides with n zero crossings in the vertical for
57 horizontal velocities.

58 **b) Energy budget: Generation, propagation and dissipation**

59
60 The generation, propagation, and dissipation of the barotropic and baroclinic tide is investigated
61 with the time-averaged and depth-integrated barotropic and baroclinic energy equation (Niwa
62 and Hibiya, 2004; Carter et al., 2008; Nagai and Hibiya, 2015, Simmons et al., 2004; Buijsman et al.,
63 2017). In each barotropic and baroclinic equation, the depth-integrated energy (E) is partitioned
64 into tendency, flux divergence, non-linear advection, barotropic to baroclinic conversion, and
65 dissipation. We can ignore the rate of change term since the short averaging period (3-months
66 and 3-years) makes this term orders of magnitude smaller than the other terms. Similarly, the
67 non-linear advection terms are assumed to be small in both the barotropic and baroclinic
68 equations (Simmons et al., 2004; Buijsman et al., 2017). This means that little energy is
69 transferred between tidal harmonics. The equations can then be written:

$$30 \quad \nabla \cdot \mathbf{F}_{bt} + D_{bt} + C = 0 \quad (1)$$

$$31 \quad \nabla \cdot \mathbf{F}_{bc} + D_{bc} - C = 0 \quad (2)$$

32
33
34 Where bt indicates the barotropic term and bc indicates the baroclinic terms, $\mathbf{F}=(F_x; F_y)$ are the
35 fluxes in the x and y directions. Dissipation (D) is computed as the residual of the flux divergence
36 and conversion (C) terms. The conversion term is identical in the barotropic and baroclinic

equations; and it appears as a sink in the barotropic equation and a source in the baroclinic equation. It is defined as in Kelly and Nash (2010):

$$C = \nabla h H \cdot \overline{\mathbf{U}_{bt} p_{bc}}|_{z=H+\eta} \quad [\text{W/m}^2] \quad (3)$$

Where $\mathbf{u} = (U, V)$ is the surface-tide velocity with components U and V along the x and y directions, p_{bc} is the baroclinic pressure, the overbar indicates a tidal average, $z = H$ defines the bottom, ∇h is the horizontal gradient ($\partial x, \partial y$) operator. $(\nabla_h \cdot)$ is the divergence operator, and η is the surface elevation.

The propagation of barotropic and baroclinic tides are examined through the divergences of the barotropic (F_{bt}) and baroclinic (F_{bc}) energy flux defined as in Nagai and Hibiya (2015):

$$\nabla \cdot \mathbf{F}_{bt} = \nabla_h \cdot \int_H^\eta \overline{\mathbf{U}_{bt} p_{bt}} dz \quad [\text{W/m}^2] \quad (4)$$

$$\nabla \cdot \mathbf{F}_{bc} = \nabla_h \cdot \int_H^\eta \overline{\mathbf{U}_{bc} p_{bc}} dz \quad [\text{W/m}^2] \quad (5)$$

Where ∇_h is the horizontal divergence.

c) Calculating (non) phase-locked internal tides

For each 3-month period of hourly time series corresponding to the January- March (JFM) 1998 El Niño and the April-June (AMJ) 1999 La Niña, the simulated time series are first harmonically analyzed to obtain the amplitude and phase of the main diurnal (K1, O1, P1) and semidiurnal (M2, K2, S2, N2) components. Then linear tidal frequency motions of vertical displacement and horizontal velocity are projected onto the barotropic mode ($n=0$) and the nine first orthogonal vertical modes ($n = 1, 2, \dots, 9$). This provides the description of the barotropic tide (mode 0) and the phase-locked baroclinic tide that can be analyzed for each mode or as the sum of the 9 baroclinic modes. These harmonic analyses provide only the tidal signal that is coherent with the astronomical forcing over each 3-month period. But several mechanisms can contribute to incoherent tides such as changes in stratification, interactions with the mesoscale flows and the internal wave field (Buijsman et al., 2017). A proxy for the incoherent part of the internal tide is to filter the signal for periods < 24 hr once the stationary, phase-locked tides have been subtracted. This incoherent or non-phase-locked component also includes the internal wave field and very rapid ocean circulation. However, the variance of the corresponding SSH field in the simulation without tides is quite small (Tchilibou et al., 2018; their Fig. 9) so in our region, the non-phase-locked component is mainly a tidal signal in the simulation with tides.

3. Contrasting El Niño/La Niña conditions

This section presents the Solomon Sea circulation, its variability, and its vertical stratification for the three year daily simulations, and for the two extreme ENSO periods: the JFM 1998 El Niño and the AMJ 1999 La Niña. All of these dynamical elements may influence the internal tide fields from its generation to its propagation and dissipation. In the western Pacific, El Niño and summer (JFM) conditions both raise the thermocline closer to the surface, La Niña and fall (AMJ) conditions have a deeper thermocline. Inspection of the model velocity and temperature showed that most of the circulation and stratification changes between these two periods are not due to the different phases of the mean seasonal cycle (not shown).

3.1 Circulation and EKE

38
39 The interannual variability of the surface circulation in R36Td is consistent with previous studies
40 on ENSO cycles (Hristova and Kessler, 2011; Melet et al., 2013) (Fig. 2). At ENSO timescales, the
41 LLWBCs transport tends to counterbalance the interior geostrophic transport. During the 1998 El
42 Niño period, the NGCC/NGCU intensifies and increases the transport towards the equator to
43 counterbalance the equatorial discharge (Fig. 2a). During the 1999 La Niña period, the
44 strengthening of the trade winds increases the SEC intensity in the equatorial band, and the
45 inflow transport at Solomon Strait. Some model experiments suggest that the induced circulation
46 anomalies in the Solomon Sea are not symmetric between the two ENSO states. This may be due
47 to the bathymetric control at the narrow Vitiaz Strait that limits the outflow of the stronger
48 NGCC during El Niño, whereas the additional inflow through the wider Solomon Strait flows more
49 freely during La Niña when the NGCC weakens (Melet et al., 2013).

50
51 A consequence of this asymmetry is a level of surface Eddy Kinetic Energy (EKE) that varies
52 strongly between the two ENSO states, as shown on the mean EKE maps representative of the
53 different 3-month periods (Fig. 2). During the El Niño case, despite the increase in LLWBC
54 transport, the level of EKE is relatively low. However, during the La Niña case, the strong shear
55 between the NGCC and the SSI (Solomon Strait Inflow) is at the origin of a high level of EKE as
56 described in Gourdeau et al. (2014). Therefore, the mean circulation and the EKE level of these
57 two contrasted periods provide different background conditions for the interactions between
58 currents and internal tides.

59 60 **3.2 SSH variability**

61
62 SSH variability, as measured by altimetry, is a good proxy of energetic motions. In the tropics, the
63 SSH wavenumber spectral signature of mesoscale variability is highly impacted by the signature
64 of internal tides for scales up to 250-300 km (Tchilibou et al., 2018). This complicates the analysis
65 of these spatial scales with a mix of mesoscale dynamics and internal tides, for all altimetric SSH
66 observations and in the context of the future SWOT mission. This new swath-altimetry mission
67 will be a great opportunity to study the 2D interactions between both dynamics in the tropics.
68 The objective of this subsection is to give some insight on the SSH variability associated with
69 mesoscale activity and internal tides in the Solomon Sea.

70
71 The largest SSH variability in the Solomon Sea is at seasonal and interannual time scales in
72 response to large-scale and low-frequency atmospheric forcing, and is responsible for up to 80%
73 of the gridded AVISO altimetric signal variance (Melet et al., 2010b; Gourdeau et al., 2014). These
74 longer time scales have an EKE level reaching $2000 \text{ cm}^2 \text{ s}^{-2}$ (Fig. 4 in Melet et al., 2010) that is of
75 same order as the intraseasonal EKE level during the La Niña period, as shown in Fig. 2b from the
76 R36Th simulation.

77
78 The SSH variability associated with the intraseasonal EKE described above is a mix of mesoscale
79 variability down to sub-inertial frequencies, and internal waves at super-inertial frequencies
80 (Savage et al., 2017). The super-inertial frequency range corresponds mostly to internal tides
81 signatures as confirmed by the quasi null SSH variability in the simulation without tides for such
82 frequency range (not shown). Figure 3 shows how the SSH standard deviation of the R36Th
83 outputs changes between the El Niño and La Niña periods for the full signal, the mesoscale
84 component ($> 48 \text{ hr}$), and the high-frequency component dominated by internal tides ($< 48 \text{ hr}$).
85 The variability of the incoherent part of the internal tides discussed in the next section is also
86 plotted.

87
88 Outside the Solomon Sea, the patterns of SSH variability are similar between the two ENSO
89 states, although there is more mesoscale energy during El Niño (Fig. 3a, b). Increased variability is

30 associated with instabilities of the GPC when it turns eastward at PNG coast near 12°S, 148°E,
31 and with instability from the SECC-SEC current system east of the Solomon Islands near 8°S,
32 164°E (Qiu and Chen, 2004). Inside the Solomon Sea, the patterns of SSH variability differ greatly
33 between the two ENSO states by a factor of 2-3. The El Niño period is marked by low variability
34 with small scale structures, compared to the La Niña period where high variability occupies the
35 central Solomon Sea, in accordance with the EKE signal (Fig. 2). During the El Niño period, the
36 level of mesoscale variability is of the same order of magnitude as the internal tides (Fig. 3c,e).
37 This explains why the full signal is composed of small structures mixing both mesoscale activity
38 and internal tides. The most energetic internal tides signal is concentrated in the Solomon Sea
39 from the southern tip of PNG to Solomon Strait (described more in section 4). Incoherent tides
40 are ubiquitous, mainly in the northern Solomon Sea. During the La Niña period, the mesoscale
41 variability is largely dominant compared to the internal tides signature (Fig. 3d, f). Note that the
42 patterns of internal tides differ slightly between both ENSO states with a more continuous
43 pattern crossing the Solomon Sea, and a substantial signature of incoherent internal tides in the
44 northern Solomon Sea during La Niña. This suggests potential interaction between mesoscale
45 dynamics and internal tides, with a possible effect on changes in water mass stratification
46 depending on the ENSO phase. This will be explored more in sections 4 and 5.

3.3 Water masses and Stratification

47
48
49
50 Internal tides are sensitive to ocean stratification and such stratification is susceptible to be
51 modified at ENSO time scales because of temperature and salinity anomalies of the different
52 water masses entering the Solomon Sea (Melet et al., 2013). Because the internal tide
53 propagates mainly in the meridional direction across the central Solomon Sea (e.g. section 4), the
54 section at 154°E is used to investigate and validate the water mass characteristics, and to
55 illustrate the corresponding stratification changes in different ENSO conditions.

56
57 First, the averaged salinity section from the 3-year R36Td is compared with that of the long-term
58 CARS climatology (Fig. 4a, b). Our model with tides shows a good positioning of the maximum
59 salinity of the SPTW waters ($\sigma_\theta=24.5 \text{ kg m}^{-3}$, $z\sim 150 \text{ m}$), and of the minimum of salt of the AAIW
60 waters ($z\sim 800\text{m}$) (e.g. section 1).

61
62 To illustrate the role of the ENSO cycle in the vertical heaving of this mean structure, the salinity
63 anomalies for El Niño and La Niña periods from R36Td are calculated with reference to the
64 complete period (Fig. 4c, d). The main changes in salinity concern the first 500 m below the
65 surface, and particularly the upper thermocline waters ($23.3<\sigma_\theta<25.7 \text{ kg m}^{-3}$). These interannual
66 salinity anomalies are consistent with large scale variability due to the effect of the anomalous
67 wind stress curl that develops at ENSO timescales in the area by strongly pulling up (down) the
68 thermocline during El Niño (La Niña), and from Rossby wave propagation forced by the
69 anomalous Ekman pumping (Melet et al., 2013).

70
71 During El Niño conditions, the resulting thermocline shoaling brings fresher and colder water
72 below the thermocline water compared to neutral conditions, and saltier/warmer surface
73 waters. The opposite situation prevails during La Niña conditions, with saltier and warmer lower
74 thermocline water, and fresher/colder upper thermocline water. During La Niña conditions, the
75 saltier waters also intrude at the surface near 3°S due to the advection of central Pacific salty
76 water by the strong SSI (Gourdeau et al., 2017).

77
78 In consequence of such ENSO variability, the density sections show a more pronounced
79 thermocline shifted upward during El Niño in comparison with La Niña, particularly in the north
80 of the section (Fig. 4c, d). These density profiles reflect changes in the vertical stratification
81 represented by the Brünt Vaisala frequency (N). Figure 5 shows the mean N profiles averaged

42 along the 154°E section when averaged in latitude across the Solomon Sea. Figure 5 compares
43 the long-term CARS climatology with the R36Td simulation characteristic of the mean 3-year
44 state, as well as the two 3-month ENSO phases. First, the modeled mean N^2 profile with tides is
45 in good agreement with the CARS climatology with maximum values in the 80-150 m depth
46 range. The ENSO phases are clearly distinguishable from the mean. The La Niña period is marked
47 by a deepening of the maximum N^2 frequency extending the thermocline down to 200 m depth.
48 The situation during El Niño is very contrasted: N^2 is marked by significantly higher values and
49 stronger thermocline gradients, especially in the surface layers with a maximum value at 50 m
50 depth. Internal tides being very sensitive to these N^2 profiles, we can assume that different
51 internal tide characteristics may occur between these two periods.
52

53 **4. M₂ Tides**

54
55 In this section, the tidal signal simulated by the regional model is described using the hourly
56 outputs from R36Th. The daily-averaged 3-year R36Td model runs allow us to investigate the net
57 longer-term effects of the tides and internal tides on water mass properties, but do not allow us
58 to closely investigate the high-frequency tide signal. A first insight into the tides is through
59 temporal spectra. SSH frequency spectral density averaged over the Solomon Sea is shown in
60 Figure 6a. Both models with and without tides agree well at low frequency ($T > 30$ hr). The
61 simulation with tides shows large peaks at diurnal and semidiurnal frequencies, and an energetic
62 supertidal band ($T < 12$ h). The tidal signal is a mixture of barotropic and baroclinic components,
63 and the SSH variance is largely dominated by the former with K1 as the main barotropic
64 component (Tchilibou, 2018).
65

66 The modal decomposition is done for each of the two ENSO phases using R36Th. To infer the
67 baroclinic tidal signature ($n \geq 1$) the barotropic tide ($n=0$, BT) is removed (Tides-BT). The
68 frequency spectra of the Tides-BT SSH signal, averaged over the Solomon Sea, shows that the
69 main baroclinic tide is at M2 period for both ENSO phases (Fig. 6b). Therefore in the following,
70 our focus will be on the dominant M2 baroclinic component. There are small differences in the
71 amplitudes of the components between the two ENSO phases, especially for semi-diurnal
72 frequencies (Fig. 6b; note that to clearly distinguish their peaks the El Niño spectrum is shifted in
73 period by two hours). The amplitude differences may be due to changes in circulation and
74 mesoscale activity as well as in stratification. The first nine baroclinic modes that we compute
75 from our model represent more than 90% of the baroclinic energy for both ENSO phases. But
76 before we analyze the baroclinic tidal components further for the two ENSO conditions, we will
77 assess how well the barotropic component has been simulated.
78

79 **4.1 M₂ Barotropic tide**

80
81 The realism of the simulated barotropic tides is crucial for the ability of the model to generate
82 realistic internal tides. The barotropic M2 tide simulated by our model is estimated for each of
83 the 3 month ENSO periods, and both estimations provide similar results (not shown). The
84 simulated barotropic M2 tide is forced at the open boundary by FES2014. Its free evolution
85 within the Solomon Sea compares well with the FES2014 solution. The M2 barotropic tide is
86 maximum outside the Solomon Sea and almost null within the Solomon Sea (Fig. 7). East of the
87 Solomon Islands, the lines of constant M2 phase in Figure 7 illustrate a southward propagation
88 that turns westward at the southern tip of the Solomon Islands with a magnitude that decreases
89 from 30 to 15 cm. The M2 barotropic tide interacts clearly with bathymetry at Solomon Strait (5°-
90 6°S), at the southern extremity of the Solomon Islands and at the southeastern tip of PNG (Fig.
91 7). The interaction of this barotropic tide with the topography enclosing the Solomon Sea is
92 favorable for generating M2 internal tides.

4.2 M2 baroclinic tide

Following the method described in section 2.2c, we access only the coherent part of the internal tide that has the advantage to be predictable, and can thus provide a SSH correction for altimetric measurements. Here we describe the dominant M2 phase-locked internal tide, in its depth-integrated form (combining the 9 baroclinic modes).

a) SSH validation of the phase-locked component

An estimate of the SSH amplitude of the M2 stationary or phase-locked baroclinic tide based on more than 20 years of altimeter measurements is given in Ray and Zaron (2016). Their result is shown in Figure 8a. The altimetric M2 baroclinic tide has a strong amplitude in the Solomon Sea, extending from the Solomon Strait in the north to the eastern tip of PNG. The amplitude of the baroclinic (coherent) tide is of the order of 3-5 cm in the Solomon Sea with an approximate wavelength of 150 km. The M2 internal tide estimated by the model during the 3-month La Niña period (Fig. 8c) is consistent with that estimated from the 20 years of altimetry, but with higher amplitudes at Solomon Strait. The M2 internal tide estimated during the El Niño period has shorter wavelengths and more dispersion over the entire domain of the Solomon Sea. Both patterns of the M2 coherent baroclinic tide resemble the full signal of internal tides calculated over these 3-month periods (Fig. 3), illustrating that M2 is the main contributor to the internal tide variability. Indeed, the M2 tide semi-diurnal tide corresponds to more than 70% of the full internal tide variance within the Solomon Sea.

The large internal tide differences between the two ENSO states raise the question of the predictability of the stationary internal tide when the level of mesoscale activity and the stratification change at interannual time scales. Note that it is during the La Niña condition when the mesoscale activity is high (e.g. Fig. 3) that the M2 internal tide appears well organized in accordance with the altimetric estimation. One explanation is the deeper stratification during La Niña is closer to the long-term mean stratification, compared to El Niño (e.g. Fig. 5). The M2 baroclinic tide is dominated by mode 1 during La Niña whereas the higher modes have increased energy during El Niño. This could also explain why the spatial pattern of the long-term coherent baroclinic M2 tide of Ray and Zaron (2016) looks like the modeled results for the La Niña period.

Mesoscale activity also influences the characteristics of baroclinic tides. Indeed, the part of coherent baroclinic tides versus the incoherent part varies substantially between the two ENSO states. During El Niño, when the LLWBCs are strong and stable and dominate the circulation, the coherent baroclinic tides explains 67% of the variance of the full internal tides. Whereas during La Niña, when the mesoscale activity is stronger because of the interactions between the LLWBCs and the SSI (Solomon Strait Inflow), only 50% of the baroclinic tide is coherent. This is clearly shown on the maps of incoherent baroclinic tides (Fig. 3) where stronger incoherent baroclinic tides are present in the northern Solomon Sea basin during the La Niña period.

b) Generation, propagation and dissipation

The distribution of the baroclinic energy flux, the energy conversion rate, the divergence of the baroclinic energy flux, and the baroclinic energy dissipation are all shown in Figure 9 for the M2 harmonic, for both the La Niña and El Niño periods. Table 1 also provides the area integrals of the different terms of the energy equation at the different generation sites as defined by the boxes on Fig. 9f for the two ENSO phases.

14 For both ENSO phases, the M2 barotropic energy flux comes from the Equatorial Pacific and
15 flows southward in the southwestern Pacific, east of Solomon Island and then turns westward
16 south of the Solomon Sea. There are two main pathways for the M2 tide to enter the Solomon
17 Sea, either by the Solomon Strait or by the southern portal. On its way it encounters three main
18 complex bathymetric features that generate intense internal tides: The Solomon Strait (5°-6°S),
19 the southern extremity of the Solomon Islands and the southeastern tip of PNG. They are the
20 three main areas of baroclinic tide generation as shown by the negative values of the energy
21 conversion rate (the sign is consistent with it being a sink term in the barotropic equation) (Fig.
22 9a,b). Weaker internal tides are also found within the Solomon Sea over the seamounts
23 extending eastward from the Woodlark archipelago (~9°S - 155°E).
24

25 Strong baroclinic energy fluxes originate in regions where significant energy conversion is
26 occurring (Fig. 9c, d). The excited baroclinic energy radiates away from the generation zones, and
27 the largest fluxes are contained within two beams: one propagating inside the Solomon Sea and
28 the other one propagating outward into the open ocean. The main baroclinic energy flow
29 entering the Solomon Sea comes from the southeastern tip of PNG where it propagates to the
30 northwest, and from the Solomon Strait where it propagates to the southwest. Both fluxes cross
31 the Solomon Sea between 153°E and 156°E. This description is in accordance with the SSH
32 signature of the M2 baroclinic tide (Fig. 8).
33

34 Estimates for the dissipation of internal tides (Fig. 9e,f) in the model are made as a residual
35 between the divergence of the baroclinic flux (Fig. 9c,d) and the conversion rate (Fig. 9a,b)
36 following equation (2). This equation does not take into account the non-linear advection
37 (Buijsman et al. 2017) that might be contained in the dissipation estimate. This might
38 overemphasize the energy of the dissipation estimate. It is interesting to note that most of the
39 dissipation occurs locally near the generation sites (Table 1), although some energy is dissipated
40 along the main propagation pathway between 152- 156°E, especially in the northern Solomon
41 Sea.
42

43 Some modulations are noted between the El Niño and La Niña periods, with a slightly stronger
44 conversion rate, stronger local dissipation and stronger energy flux during the El Niño period. The
45 dissipation is also quite significant during La Niña in the northern Solomon Sea, away from the
46 generation site (Figure 9, Table 1).
47

48 **c) Quantification of the tidal energy budget for the two ENSO states**

49

50 For the Solomon Strait box (Fig. 9f, red), the divergence of the barotropic flux energy is around 3
51 GW (Table 1). The majority of this flux divergence is converted into baroclinic tides (~ 70%, ~ 2.10
52 GW) with the bottom friction (barotropic dissipation) accounting for ~ 0.85 GW. The majority of
53 the energy converted from barotropic to baroclinic energy is dissipated within the box, but there
54 is stronger local dissipation during El Niño (75%) than during La Niña (66%). So we observe a
55 stronger baroclinic energy flux radiating out of the box during the La Niña period that may
56 dissipate in the far field. 0.7 GW radiates out of the box as a baroclinic flux during the La Niña
57 period compared to 0.55 GW during El Niño. More than half of this energy propagates into the
58 Solomon Sea.
59

60 For the box representative of the southern extremity of the Solomon archipelago (Fig. 9f, blue),
61 the divergence of the barotropic flux energy is around 6 GW, twice that of the Solomon Strait
62 box. The majority (~ 60%) of this flux divergence is converted into baroclinic tides (4 GW) with
63 the bottom friction (barotropic dissipation) accounting for 2 GW. The majority of the energy
64 converted from barotropic to baroclinic energy is dissipated within the box and the dissipation
65 rate varies from 70% to 80% between El Niño and La Niña, respectively. During the El Niño event,

26 the barotropic flux divergence is larger than during the La Niña event (6.83 vs 5.89 GW). In
27 consequence, the conversion rate is stronger in the same proportion (Table 1), but the
28 dissipation is identical between the two ENSO events (~3GW). The baroclinic flux radiating out of
29 the box increases during El Niño (1.27 GW compared to 0.75 GW during La Niña) meaning that
30 more dissipation must occur in the far field during El Niño. Most of this baroclinic energy radiates
31 out of the Solomon Sea, and only 0.24/0.17 GW radiates into the Solomon Sea during the El
32 Niño/La Niña periods.

33
34 The PNG box (Fig. 9f, green) is smaller than the other boxes, and the divergence of the barotropic
35 flux energy is around 1.8 GW. More than 75% of this flux divergence is converted into baroclinic
36 tides (1.36 GW). The majority of the energy converted from barotropic to baroclinic energy
37 radiates out of the box (0.75 GW), and 0.22 GW radiates into the Solomon Sea. No contrasted
38 situations are observed between the two ENSO phases.

39
40 In summary, there are three areas where a large part of the barotropic flux energy is converted
41 into baroclinic energy (63 to 79%). Most of the excited baroclinic energy is dissipated locally (46
42 to 80%), and only two generation sites at Solomon Strait and at the Southeast extremity of PNG
43 radiate significant baroclinic tidal energy into the Solomon Sea. Solomon Strait radiates most of
44 the baroclinic energy into the Solomon Sea, especially during the La Niña state with a 27%
45 increase of the energy flux compared to El Niño. Most of this baroclinic energy is dissipated in
46 the northern Solomon Sea as illustrated by Figure 9f, with higher dissipation here during La Niña
47 compared to El Niño. This is likely to be impacted by the contrasted circulation and mesoscale
activity in this area between the El Niño and La Niña periods. The strong northward LLWBC
current exiting the Solomon Sea during El Niño is replaced by the southward SSI current during
the La Niña period (see Fig. 2) that favors the advection of the tidal baroclinic energy inside the
Solomon Sea. Also, the higher EKE level during La Niña than during El Niño (Fig. 2) favors stronger
interactions between eddies and internal tides. This appears to render the internal tide more
incoherent (e.g. Fig. 3gh) and to increase the tidal dissipation (Fig. 9f). At the Southeast extremity
of PNG (Fig. 9f, blue) crossed by the strong NGCU, the tidal baroclinic energy exhibits no
contrasted situations between the two ENSO phases.

27 **d) Vertical signature**

28
29 In the previous sections, baroclinic tides were investigated by considering their depth-integrated
30 form. For a more quantitative discussion on the vertical structure of the propagating M2
31 baroclinic tide, we perform modal decomposition of the model-predicted baroclinic energy
32 fluxes. Figure 10 shows the spatial distribution of the M2 modes 1 and 2 for the El Niño and La
33 Niña states. These two modes account for almost the entire variance of the full baroclinic M2
34 energy flux. Mode 1 is the dominant mode (note the different scales between mode 1 and 2).
35 However, Mode 2 is particularly present within the Solomon Sea during the El Niño period,
36 compared to the La Niña period where Mode 2 energy is locally dissipated at the generation
37 sites. An explanation for such a difference is the change in stratification between the two ENSO
38 states, with stratification being closer to the surface during El Niño that favors the excitation of
39 higher order modes (Fig. 5).

40
41 Whatever the ENSO state, Mode 1 energy flux propagates into the Solomon Sea, from Solomon
42 strait and from the southeastern tip of PNG. The PNG flux is relatively stable (see Table 1) and
43 follows the NGCU pathway until the Woodlark Archipelago (9°S). Whereas the Solomon Strait
44 flux exhibits strong changes in propagation between the two ENSO states that appear related to
45 the background circulation. During El Niño, this Mode 1 flux is directed to the South West in the
46 lee of the LLWBC exiting at Solomon Strait. It breaks into two branches when encountering the
47 northward NGCC to the West. During La Niña, the flux is southward in the wake of the Solomon

48 Strait inflow. This suggests the constraint of the propagation of the baroclinic tidal energy by the
49 background circulation. The mode 1 baroclinic flux emanating from the south Solomon Sea is less
50 intense during La Niña (Table 1) and this flux exits the Solomon Sea to the South.

51
52 To illustrate the changes brought by the stratification and the circulation on the vertical structure
53 of the M2 baroclinic flux, we show a vertical section along 154°E of the meridional baroclinic
54 energy fluxes for the two ENSO phases (Fig. 11). This section transects the prominent baroclinic
55 energy flux in the Solomon Sea. The highest energy fluxes are located in the upper 300 m depth
56 but they extend deeper during the La Niña period than during El Niño in accordance with
57 changes in stratification (Fig. 5). During El Niño, when the NGCC/NGCU are strong, the northward
58 baroclinic energy flux from the southern tip of PNG crossed practically all the Solomon Sea up to
59 6.5°S. During La Niña, when the SSI is strong, the baroclinic energy flux from the Solomon Strait
60 extends to the south and the southward and northward fluxes meet in the central Solomon Sea
61 (8°S).

62
63 In summary, the M2 baroclinic energy flux is concentrated in the upper 200-300m depth.
64 Propagation, and depth penetration of this energy vary between the two ENSO states depending
65 on the background circulation and stratification. Mode 1 accounts for most of the propagation of
66 the energy flux but Mode 2 is also significant, particularly during the JFM El Niño period
67 characterized by a stratification close to the surface.

68 **5. Tidal effect on water mass transformation**

69
70 Here, we take advantage of our 3-year R36d twin simulations, forced with tides (TIDE) and
71 without tides (NOTIDE), to analyze the net impact of internal tides on the Solomon Sea's water
72 mass modification. Most of the transformation occurs in the SW ($\sigma\theta < 23.3 \text{ kg m}^{-3}$), UTW ($23.3 <$
73 $\sigma\theta < 25.7 \text{ kg m}^{-3}$), and IW ($26.7 < \sigma\theta < 27.5 \text{ kg m}^{-3}$) water masses. We recall that the salinity
74 maximum of the SPTW waters in the UTW is the key variable that impacts on the T-S
75 modifications on the EUC. Whereas the SWs, which feed into the west Pacific warm pool, can
76 modulate the critical air-sea interactions there. At depth, the IW influences the water mass
77 properties of the cross-equatorial intrusion, in turn impacting on the North and equatorial
78 Pacific's overturning circulation (Qu and Lindstrom, 2004).

79
80 This section will firstly address the long-term impacts of internal tides on the SW, UTW and IW,
81 based on the daily outputs from the 3-year simulations. Secondly, the transit time for the SW
82 waters are short enough (e.g. Melet et al., 2013) to allow us to investigate any sensitivity of the
83 internal tide on the SW properties during our contrasting ENSO conditions.

84 **a) Long term changes between TIDE and NOTIDE simulations**

85
86 Salinity is a key parameter defining the water mass extrema. The mean salinity distribution of
87 UTW waters shows the intrusion of the high salinity SPTW water in the Solomon Sea on Figure 12
88 for the 3- year NOTIDE and TIDE simulations compared to the CARS climatology. This high salinity
89 tongue is firstly advected westward by the NVJ at 11°S before joining the NGCU around 155°E. As
90 it continues to be carried northward into the Solomon Seas, it is eroded along its route.
91 Interactions between the NGCU and the bathymetry, as well as the merging of the different
92 currents, and the effects of tides are components that can erode the salinity maximum. The
93 models with and without tides and the CARS data all show a strong erosion at the entrance of
94 the Solomon Sea with a 0.06 psu freshening between the southeastern extremity of PNG and the
95 Woodlark archipelago at 9°S. The salinity erosion is enhanced in the TIDE simulation compared to
96 the NOTIDE simulation, and erosion is also visible in the northern Solomon Sea along the NGCU
97 pathway. We note that the mean N^2 profile along the axis of this high salinity tongue at 154°E
98

99 (Fig.5) had already highlighted the closer resemblance of the UTW in the CARS and TIDES
100 simulations compared to the NOTIDES simulation.

101
102 Another difference between the TIDE and NOTIDE simulations concerns the zonal salinity
103 gradient between the high salinity tongue carried by the LLWBCs and the lower UTW salinity
104 along the Solomon Islands. This zonal salinity gradient within this isopycnal UTW layer is
105 enhanced in the TIDE simulation, suggesting that tides induce diapycnal mixing that is particularly
106 efficient in the eastern and northern parts of the Solomon Sea. These regions where mean
107 currents and EKE are relatively low (eastern Solomon Sea) and where strong recirculation exists
108 (northern Solomon Sea) could be favorable to tidal mixing because of longer transit time for
109 particles here.

110
111 The strong zonal salinity gradient in the TIDE simulation is also visible in the CARS climatology,
112 although a fresh bias of about 0.02 psu may be noted in the TIDE simulation compared to CARS.
113 This comparison with the long-term CARS climatology has some limitations with regard to the
114 particular conditions of our 3-year simulation including strong El Niño and La Niña events. We
115 note that CARS shows a strong salinity maximum around 5°S outside and to the east of the
116 Solomon Sea that does not match our 3- year period simulations, where this salinity maximum in
117 the open ocean has a bias and is shifted to the south around 11°S. We have verified that the
118 UTW salinity averaged over the same period as our simulations based on a monthly gridded T-S
119 data (CORA05; Cabanes et al., 2013), also exhibits such a southward shift (not shown).
120 Unfortunately, CORA05 has few observations available inside the Solomon Sea, since it is based
121 mainly on ARGO data. So we can perform interannual validations outside the Solomon Sea, but
122 inside the sea only long-term comparisons are possible.

123
124 Temperature and salinity changes between the NOTIDE and TIDE simulations are presented in
125 Figure 13 for the different water masses. The difference between these 3-year simulations shows
126 that tidal mixing reduces the T/S extrema, and induces cooler and saltier SW, cooler and fresher
127 UTW, and warmer and saltier IW. It means that the corresponding salt flux is transferred
128 downward to IW, and upward to SW. In the same way, the diapycnal mixing from tides at the
129 thermocline level induces a heat flux that cools the UTW and SW, and warms the IW. This results
130 in a weaker stratification at the thermocline level in the TIDE simulation compared to the NOTIDE
131 simulation (e.g. Fig. 5).

132
133 The largest impact of the tides is for the UTW layer, and the tide effect is strongest along the
134 Solomon Islands with fresher salinity up to -0.08 psu and colder temperature up to -0.3°C for the
135 TIDE simulation. But when averaged over the Solomon Sea, the rectified anomalies due to the
136 tides are only of -0.04 for salinity and -0.1°C for temperature. The salt and heat fluxes in the TIDE
137 simulation impact the SW and IW waters to a lesser effect, again with the highest differences
138 along the Solomon Islands. Once again, when averaged over the Solomon Sea, the rectified
139 anomalies due to the tides are only of -0.06°C (0.08°C) for temperature and of 0.0 1 for salinity
140 for IW and SW, respectively, although locally the differences may reach 0.9°C and 0.15 psu (Fig.
141 13).

142
143 At the surface, the cooling of SW by the tides could affect the SST field that in turn affects the
144 latent heat flux and the corresponding net heat flux (Q_{net}). This corresponds to a positive Q_{net}
145 anomaly between the simulation with and without tides that matches the pattern of SW
146 temperature difference in Figure 13, and represents a 15% increase in Q_{net} when tides are
147 included. This Q_{net} increase acts to reduce the SST cooling induced by internal tides. Averaged
148 over the Solomon Sea, the SST cooling due to the tides is -0.06°C for SW, and only -0.04°C at the
149 surface. This is an order of magnitude less than the SST cooling in the Indonesian Seas that

50 drastically affects the overlying deep atmospheric convection when modeled in a coupled ocean-
51 atmosphere model including a tidal parameterization (Koch-Larrouy et al. , 2010).
52

53 **b) Sensitivity to extremes conditions**

54 The mean tidal effect on water mass transformation is rather modest, but we can ask if extreme
55 conditions like ENSO events impact on the role of tides on water mass transformation because
56 internal tides are sensitive to contrasted ENSO periods (e.g. section 4). To illustrate this point, we
57 focus on the 3-month periods of El Niño and La Niña, and we concentrate on SW waters since the
58 transit time of SW waters is short enough to be influenced by these extreme conditions (Melet et
59 al., 2011). Fig. 14 shows the temperature differences of SW between the TIDE-NOTIDE
60 simulations for the two ENSO periods, calculated relative to their 3-year mean. The tidal impact
61 on SWs during the ENSO period is quite small, with maximum differences in the Solomon Sea
62 reaching +/- 0.15°C between the TIDE and NOTIDE simulations. The tide-induced temperature
63 differences are weaker in the La Niña case with a temperature difference of 0.018°C compared to
64 0.05°C for the El Niño case when averaged over the Solomon Sea. These values are of the same
65 order as the mean tidal effect (e.g. 5b) but they are an order of magnitude smaller than the
66 temperature changes introduced by the circulation and stratification changes between the El
67 Niño and La Niña cases (0.8°C, e.g. 5a).

68 Indeed, the differences between the two ENSO states are strongly related to the circulation
69 anomalies. During El Niño, the LLWBC strongly increases in both simulations, and we observe
70 maximum positive temperature differences due to the tides along its pathway (Fig. 14a). In the
71 same way, during La Niña maximum positive differences are present along the Solomon Islands
72 where the SSI (Solomon Strait Inflow) turns and flows strongly southward (Fig. 14b). Since these
73 positive temperature anomalies are relative to the 3-year mean cooling of SWs (Fig. 13) by the
74 tides, they highlight that the intense circulation changes during the ENSO periods lead to a
75 reduced effect of the tides on the SW waters. In other words, the tidal effect will be more
76 efficient when the circulation has lower energy.
77

78 **6. Discussion/Conclusion**

79
80 We have analyzed here the role of internal tides in the Solomon Sea and their impact on the
81 circulation and the surface and subsurface water masses, based on two regional simulations with
82 and without tides. Since the interaction of the internal tide with the background circulation has
83 strong nonlinear interactions, and the energy cascade between them can cover similar space-
84 time scales, it is not easy to cleanly separate the two signals from a single model. In our model
85 set-up, having 2 distinct models with and without tides but with the same resolution and surface
86 forcing has allowed us to more easily explore the impacts of introducing the barotropic and
87 baroclinic tides into a regional circulation model, for both the phase-locked and non phase-
88 locked components.
89

90 Since the Solomon Sea is influenced by ENSO, the characteristics of the internal tides were
91 analyzed for two contrasted ENSO conditions: the JFM 1998 El Niño and the AMJ 1999 La Niña.
92 These are two extreme events with strong stratification changes in the western Pacific and
93 Solomon Seas, and provide good case studies for investigating the impact of the internal tides on
94 the regional circulation and water mass transformation. We are conscious though that we have
95 only analyzed one El Niño and one La Niña event, each over a limited 3-month period of hourly
96 averages, which is insufficient to conclude on the influence of ENSO on the internal tides. Indeed,
97 3-months is roughly twice the mesoscale eddy decorrelation time in the tropics but it is also the
98 local residence time for surface waters flowing through the Solomon Sea (Melet et al, 2011). A
99 longer simulation, including more contrasted El Niño/La Niña events, would be needed to better
100 characterize the response of the tides to the ENSO variability. Nevertheless, these two

01 contrasted events are sufficiently different to qualitatively describe the changes induced in the
02 internal tide field.
03

04 Within the Solomon Sea, the M2 barotropic tide is rather weak but its interaction with the strong
05 topographic features (islands, shelves, deep ocean ridges) generates the strongest component of
06 the internal tide. Although the M2 Mode 1 is the dominant mode to propagate baroclinic tidal
07 energy within the Solomon Sea, during the JFM El Niño period, when the peak in N^2 stratification
08 is close to the surface, more energy becomes partitioned into mode 2. This is important since
09 studies that aim to predict and remove the internal tide from altimetric SSH observations, before
10 calculating geostrophic currents, may use an empirical "all mode" fitting of the M2 internal tide
11 (eg Ray and Zaron, 2016) or concentrate only on mode 1 (Zhao et al., 2016). In this Solomon Sea
12 region, with strong stratification changes, we need at least modes 1 and 2.
13

14 We have concentrated on this M2 component for our study, to simplify the presentation, but
15 other modes are also energetic (S2, M4, K1, O1; Figure 6). The second highest baroclinic tide
16 mode is S2, which is well observed by the current Topex/Jason altimeter orbits and also in the
17 future SWOT mission, whose orbit is designed to characterize the 2D structure of the tides and
18 internal tides (Fu et al., 2009; Morrow et al., 2019). Other altimeters on a sun-synchronous orbit
19 (Envisat, Saral-AltiKa, Sentinel-3, planned future wide-swath missions) will not be able to observe
20 this S2 12h cycle, which poses a problem for the understanding of the S2 internal tide, its
21 interaction with the changing ocean circulation, and the validation of models with tides in the
22 future (post SWOT). Future studies are needed to investigate the impacts of the S2 internal tide
23 in the Solomon Sea and in the tropics.
24

25 We find that the generation, propagation and dissipation of the internal tides are sensitive to
26 changes in stratification and to the circulation changes and mesoscale activity that occurs
27 between these two El Niño and La Niña cases. Our AMJ La Niña case study with its high level of
28 mesoscale activity and deeper stratification favors the appearance of more non phase-locked
29 internal tides. So it appears that the strong mesoscales are refracting, scattering and eventually
30 dissipating the internal tide field that propagated away from its generation sites, contributing to
31 the increase in the non phase-locked component.
32

33 Where and how the 1 TW of global internal tide energy is dissipated in the open ocean has also
34 been a long-standing question (Egbert and Ray, 2000). The dissipation of internal tides may occur
35 right after generation or after radiation away from the generation sites. Our analysis showed that
36 most of the dissipation in the Solomon Seas occurs locally (from 60 to 80%), but the proportion
37 of local to far-field dissipation varies during these particular El Niño or La Niña periods. For
38 example, during the La Niña period, there is a lower baroclinic tide generation in the Solomon
39 Strait box, thus less local dissipation, but an increase in the far field dissipation between 7 and
40 8°S that is quite significant. This may be influenced by the interaction of the EKE with the
41 southward propagative internal tides generated in the Solomon Strait, but highlights the
42 variability in the dynamical interactions, and the complications this introduces in the energy
43 budget estimations (see Table 1).
44

45 The description of the TIDE and NOTIDE simulations show a rather modest effect of the tides on
46 water mass transformation inside the Solomon Sea compared to the observations in Germeaud
47 et al. (2016) that show large variations of thermocline water properties (up to 0.2 psu for the
48 SPTW waters) between the different entrances and exits of the Solomon Sea. It is worth noting
49 that the property differences between entrance and exits could be due to the merging and
50 presumably mixing of the different flows with different characteristics transiting at these places.
51 These specific places correspond with the areas of internal tide generation, and most of the

52 internal tide energy is dissipated locally and could contribute to the water mixing at the entrance
53 and exits of the Solomon Sea (Fig. 12).

54
55 Water mass transformation inside the Solomon Sea had already been investigated with the use
56 of a $1/10^\circ$ regional model including a tidal parameterization and Lagrangian diagnostics during
57 neutral and ENSO conditions (Melet et al., 2011, 2013). Along the main pathways of UTW waters,
58 they show that the erosion of the salinity maximum varies from 0.07 and 0.11 psu. Such values
59 are higher than the ones due only to the tides as discussed above. This erosion may be the
60 consequence of mixing by tides and also many other processes. But they suspect that their tidal
61 mixing parametrization might overestimate the erosion of the SPTW salinity maximum.

62
63 Our modeling results show that the diapycnal mixing induced by the tides acts to erode the
64 salinity maximum of the upper thermocline water, and to cool the surface temperature
65 interacting with the atmosphere. The effect of tides on water mass mixing is modest, but is
66 stronger closer to the generation sites where most of this tidal energy is dissipated locally and
67 where different water masses merge. Tidal effects are also visible away from the strong currents,
68 where particles may experience the effect of tide during a longer time. Indeed, the impacts are
69 quite different when considering particular ENSO conditions over the shorter 3-month period.
70 For example, the stronger surface mesoscale circulation in different regions during the El Niño or
71 La Niña periods, tends to reduce the mean SST cooling by the tides, with possible effects on
72 regional air sea interactions. But the global impact of such tidal effects for this marginal sea,
73 given its key position upstream of the equatorial Pacific circulation, need to be evaluated.

74
75 Finally, we note some caveats. Our 3-month hourly simulations in contrasting ENSO conditions
76 represent examples of particular ENSO events, over one season in each case, and including a
77 slowly-varying mesoscale field. Longer simulations covering more interannual events are needed
78 to better understand how the internal tides may be modified under varying ENSO cases, and to
79 better separate the role of mesoscale variability interacting with the internal tides. We have thus
80 not attempted to quantify the energetics of these tide-circulation interactions with such short
81 time series. These short model simulations are also difficult to validate, since in-situ data are
82 scarce, and longer time series are needed to build up robust internal tidal signals from 10 or 35-d
83 altimetric sampling. Future work using longer model simulations, compared to swath
84 observations of the 2D internal tide structure from the future SWOT mission in 2022-2025,
85 should give us a more quantitative picture of the interaction of the ocean circulation and internal
86 tides in the Solomon Sea.

87 **Acknowledgements**

88 This work is part of M. Tchilibou's PhD thesis funded by the University of Toulouse III. L.
89 Gourdeau and A. Koch-Larrouy are funded by IRD; R. Morrow is funded by CNAP, F. Lyard and D.
90 Allain by CNRS and B. Djath was funded by CNES. The paper benefited from helpful discussions
91 with J. Jouanno from LEGOS, with Billy Kessler, University of Washington, and from an
92 anonymous reviewer. This work is a contribution to the joint CNES/NASA SWOT project "SWOT in
93 the tropics" and is supported by the French TOSCA programme. The NOAA/ETOPO2v2
94 bathymetric file used in the Figures is from the Smith & Sandwell database (doi:
95 10.7289/V5J1012Q).

96 **References**

97
98
99
100 Albery, M. S., Sprintall J., MacKinnon J., Ganachaud A., Cravatte S., Eldin G., Germineaud C., and
101 Melet A.: Spatial patterns of mixing in the Solomon Sea, *J. Geophys. Res.*
102 *Oceans*,122, <https://doi.org/10.1002/2016JC012666>, 2017.

- 33 Arbic, B., Wallcraft, J., Metzger, J.: Concurrent simulation of the eddying general circulation and
34 tides in a global ocean model, *Ocean Mod.*, 32(3-4), 175 – 187, 2010.
- 35 Buijsman, M. C., Arbic B. K., Richman J. G., Shriver J. F., Wallcraft A. J., and Zamudio, L.:
36 Semidiurnal internal tide incoherence in the equatorial Pacific, *J. Geophys. Res.*
37 *Oceans*, 122, <https://doi.org/10.1002/2016JC012590>, 2017.
- 38 Cabanes, C., Grouazel, A., Von Schuckmann, K., Hamon, M., Turpin, V., Coatanoan, C., Paris, F.,
39 Guinehut, S., Boone, C., Ferry, N., De Boyer Montegut, C., Carval, T., Reverdin, G.,
40 Pouliquen, S., Le Traon, P.Y.: The CORA dataset: validation and diagnostics of in-situ ocean
41 temperature and salinity measurements. *Ocean Science*, 9(1), 1-18,
42 <https://doi.org/10.5194/os-9-1-2013>, 2013.
- 43 Carrere, L., Lyard, F., Cancet, M., Guillot, A.: FES 2014, a new tidal model on the global ocean
44 with enhanced accuracy in shallow seas and in the Arctic region. *Geophysical Research*
45 *Abstracts*, vol. 17. EGU2015-5481-1, EGU General Assembly, 2015.
- 46 Carter, G.S., Merrifield M.A., Becker J.M., Katsumata K., Gregg M.C., Luther D.S., Levine M.D.,
47 Boyd T.J., and Firing Y.L.: Energetics of M2 Barotropic-to-Baroclinic Tidal Conversion at the
48 Hawaiian Islands. *J. Phys. Oceanogr.*, 38, 2205-2223,
49 <https://doi.org/10.1175/2008JPO3860.1>, 2008
- 50 Chavanne, C., Flament, P., Carter, G., Merrifield, M., Luther, D., Zaron, E., and Gurgel, K. W.: The
51 Surface Expression of Semidiurnal Internal Tides near a Strong Source at Hawaii. Part I:
52 Observations and Numerical Predictions. *J. Phys. Oceanogr.*, 40(6), 1155-1179, 2010
- 53 Cravatte, S., Ganachaud, A., Duong, Q.-P., Kessler, W. S., Eldin, G., and Dutrieux, P.: Observed
circulation in the Solomon sea from SADCP data, *Prog. Oceanogr.*, 88(1-4), 116–130,
<https://doi.org/10.1016/j.pocean.2010.12.015>, 2011
- Colosi, J. A., and W. Munk, 2006: Tales of the venerable Honolulu tide gauge. *J. Phys. Oceanogr.*,
36, 967-996.
- Davis, R. E., Kessler, W. S., and Sherman, J. T.: Gliders measure western boundary current
transport from the south pacific to the equator, *J. Phys. Oceanogr.*, 42(11), 2001–
2013, <https://doi.org/10.1175/JPO-D-12-022.1>, 2012.
- Dee, D. P., Uppala, S. M., Simmons, A. J., Berrisford, P., Poli, P., Kobayashi, S., Andrae, U.,
Balmaseda, M. A., Balsamo, G., Bauer, P., Bechtold, P., Beljaars, A. C. M., van de Berg, L.,
Bidlot, J., Bormann, N., Delsol, C., Dragani, R., Fuentes, M., Geer, A. J., Haimberger, L.,
Healy, S. B., Hersbach, H., Helm, E. V., Isaksen, L., Kallberg, P., Kahler, M., Matricardi, M.,
McNally, A. P., Monge-Sanz, B. M., Morcrette, J.-J., Park, B.-K., Peubey, C., de Rosnay, P.,
Tavolato, C., Thepaut, J.-N., and Vitart, F.: The ERA-Interim reanalysis: configuration and
performance of the data assimilation system, *Q. J. Roy. Meteorol. Soc.*, 137, 553–597,
<https://doi.org/10.1002/qj.828>, 2011.
- Djath, B., Verron, J., Melet, A., Gourdeau, L., Barnier, B., and Molines, J.-M.: Multiscale dynamical
analysis of a high-resolution numerical model simulation of the Solomon Sea circulation, *J.*
Geophys. Res.-Oceans, 119, 6286–6304, <https://doi.org/10.1002/2013JC009695>, 2014.
- Dunn, J. R., and K. R. Ridgway, K.R.: Mapping ocean properties in regions of complex topography,
Deep-Sea Res, I, 49, 591-604, doi:[https://doi.org/10.1016/S0967-0637\(01\)00069-3](https://doi.org/10.1016/S0967-0637(01)00069-3), 2002.
- Egbert, G., and Ray, R.: Significant dissipation of tidal energy in the deep ocean inferred from
satellite altimeter data, *Nature*, 405, 775 – 778, 2000.
- Fine, R. A., Lukas R., Bingham F., Warnar M., and Gammon R.: The western equatorial Pacific: A
water mass crossroads, *J. Geophys. Res.*, 99, 25 063–25 080, 1994.
- Fu, L-L., E Rodriguez, D Alsdorf, R. Morrow (eds). (2012). SWOT Mission Science document. JPL
Publication. https://swot.jpl.nasa.gov/files/swot/SWOT_MSD_1202012.pdf
- Ganachaud, A., Cravatte, S., Melet, A., Schiller, A., Holbrook, N. J., Sloyan, B. M., Widlansky, M. J.,
Bowen, M., Verron, J., Wiles, P., Ridgway, K., Sutton, P., Sprintall, J., Steinberg, C.,
Brassington, G., Cai, W., Davis, R., Gasparin, F., Gourdeau, L., Hasegawa, T., Kessler, W.,
Maes, C., Takahashi, K., Richards, K. J., and Send, U.: The Southwest Pacific Ocean

- 54 circulation and climate experiment (SPICE), *J. Geophys. Res.-Oceans*, 119, 7660–7686,
55 <https://doi.org/10.1002/2013JC009678>, 2014.
- 56 Gasparin, F., Ganachaud A., Maes C., Marin F., and Eldin G.: Oceanic transports through the
57 Solomon sea: The bend of the New Guinea coastal undercurrent, *Geophys. Res. Lett.*, 39,
58 L15608, <https://doi.org/10.1029/2012GL052575>, 2012.
- 59 Germineaud, C., Ganachaud, A., Sprintall, J., Cravatte, S., Eldin, G., Albery, M. S., and Privat, E.:
60 Pathways and water mass properties of the thermocline and intermediate waters in the
61 Solomon Sea. *J. Phys. Oceanogr.*, 46 (10), 3031–3049. ISSN 0022-3670
- 62 Gourdeau, L.: Internal tides observed at 2°S–156°E by in situ and TOPEX/POSEIDON data during
63 COARE, *J. Geophys. Res.-Oceans*, 103, 12629–12638, 1998.
- 64 Gourdeau, L., Verron, J., Melet, A., Kessler, W., Marin, F., and Djath, B.: Exploring the mesoscale
65 activity in the Solomon Sea: a complementary approach with numerical model and
66 altimetric data, *J. Geophys. Res.-Oceans*, 119, 2290–2311,
67 <https://doi.org/10.1002/2013JC009614>, 2014.
- 68 Gourdeau, L., Verron, J., Chaigneau, A., Cravatte, S., and Kessler, W.: Complementary use of
69 glider data, altimetry, and model for exploring mesoscale eddies in the tropical Pacific
70 Solomon Sea, *J. Geophys. Res.-Oceans*, 122, 9209–9229,
71 <https://doi.org/10.1002/2017JC013116>, 2017.
- 72 Grenier, M., Cravatte, S., Blanke, B., Menkes, C., Koch-Larrouy, A., Durand, F., Melet, A., and
73 Jeandel, C.: From the western boundary currents to the Pacific equatorial undercurrent:
74 Modeled pathways and water mass evolutions, *J. Geophys. Res.-Oceans*, 116,
75 C12044, <https://doi.org/10.1029/2011JC007477>, 2011.
- 76 Hristova, H. G., and Kessler, W. S.: Surface circulation in the Solomon Sea derived from
77 Lagrangian drifter observations, *J. Phys. Oceanogr.*, 42(3), 448–458,
78 <https://doi.org/10.1175/JPO-D-11-099.1>, 2012.
- 79 Hristova, H. G., Kessler, W. S., McWilliams, J. C., and Molemaker, M. J.: Mesoscale variability and
80 its seasonal variability in the Solomon and coral seas, *J. Geophys. Res.-Oceans*, 119, 4669–
81 4687, <https://doi.org/10.1002/2013JC009741>, 2014.
- 82 Kelly, S. M., and Nash, J.D.: Internal-tide generation and destruction by shoaling internal tides,
83 *Geophys. Res. Lett.*, 37, L23611, doi:10.1029/2010GL045598, 2010.
- 84 Kelly, S. M., Nash, J. D., and Kunze, E.: Internal-tide energy over topography, *J. Geophys. Res.-*
85 *Oceans*, 115, C06014, <https://doi.org/10.1029/2009JC005618>, 2010.
- 86 Kelly, S.M., Nash, J.D., Martini, K.I., Alford, M.H., and Kunze, E.: The Cascade of Tidal Energy from
87 Low to High Modes on a Continental Slope, *J. Phys. Oceanogr.*, 42, 1217–1232,
88 <https://doi.org/10.1175/JPO-D-11-0231.1>, 2012.
- 89 Kessler, W.S., Hristova, H.G., Davis, R.E., and Sherman, J.T.: Equatorward western boundary
90 transport from the South Pacific: Glider observations, dynamics and consequences. *Prog.*
91 *Oceanogr.*, 175, 208–225, <https://doi.org/10.1016/j.pocean.2019.04.005>, 2019.
- 92 Kida, S., and Wijffels, S.: The impact of the Indonesian Throughflow and tidal mixing on the
93 summertime sea surface temperature in the western Indonesian Seas, *J. Geophys. Res.*,
94 117, C09007, doi:10.1029/2012JC008162, 2012.
- 95 Koch-Larrouy, A., Madec, G., Bouruet-Aubertot, P., Gerkema, T., Bessières, L., Molcard, R.: On the
96 transformation of Pacific Water into Indonesian Throughflow Water by internal tidal
97 mixing, *Geophys. Res. Lett.*, 34, (L04604), 2007.
- 98 Koch-Larrouy, A., Lengaigne, M., Masson, S., Madec, G., Terray, P.: Indonesian tidal mixing effect
99 on climate system, *Clim. Dyn.*, <http://dx.doi.org/10.1007/s00382-009-0642-4>, 2010.
- 100 Koch-Larrouy, A., Atmadipoera, A., van Beek, P., Madec, G., Aucan, J., Lyard, F., Grelet, J.,
101 Souhaut, M.: Estimates of tidal mixing in the Indonesian archipelago from multidisciplinary
102 INDOMIX *in-situ* data, *Deep-Sea Res. I*, 106, 136 - 153, 2015.
- 103 Large, W., and Yeager, S.: The global climatology of an interannually varying air-sea flux data set,
104 *Clim. Dyn.*, 33, 341–364, 2009.

- 35 Levitus, S., Boyer, T. P., Conkright, M. E., O'Brien, T., Antonov, J., Stephens, C., and Gelfeld, R.:
36 NOAA Atlas NESDIS 18, World Ocean Data base 1998: VOLUME 1: Introduction, US Gov.
37 Printing Office, Washington, D.C., 346 pp., 1998.
- 38 Madec, G.: NEMO ocean engine, Note du Pole de Modélisation, Tech. Rep. 27, Inst. Pierre Simon
39 Laplace, France, 300 pp., 2008.
- 40 Melet, A., Gourdeau, L., Kessler, W. S., Verron, J., and Molines, J.-M.: Thermocline circulation in
41 the Solomon Sea: A modeling study, *J. Phys. Oceanogr.*, 40(6), 1302–1319,
42 <https://doi.org/10.1175/2009JPO4264.1>, 2010a
- 43 Melet, A., Gourdeau, L., and Verron, J.: Variability in Solomon sea circulation derived from
44 altimeter sea level data, *Ocean Dyn.*, 60(4), 883–900, doi:10.1007/s10236-010-0302-6,
45 2010b.
- 46 Melet, A., Verron, J., Gourdeau, L., and Koch-Larrouy, A.: Equatorward pathways of Solomon sea
47 water masses and their modifications, *J. Phys. Oceanogr.*, 41, 810–826,
48 <https://doi.org/10.1175/2010JPO4559.1>, 2011.
- 49 Melet, A., Gourdeau, L., Verron, J., and Djath, B.: Solomon sea circulation and water mass
50 modifications: Response at ENSO timescales, *Ocean Dyn.*, 63(1), 1–19,
51 <https://doi.org/10.1007/s10236-012-0582-0>, 2013.
- 52 Merrifield, M. A., and Holloway, P. E.: Model estimates of M2 internal tide energetics at the
53 Hawaiian Ridge. *J. Geophys. Res.*, 107, 3179, doi:10.1029/2001JC000996, 2002.
- 54 Morrow, R., Fu, L. L., Arduin, F., Benkiran, M., Chapron, B., Cosme, E., D'Ovidio, F., Farrar, J. T.,
55 Gille, S. T., Lapeyre, G., Le Traon, P. Y., Pascual, A., Ponte, A., Qiu, B., Rascle, N., Ubelmann,
56 C., Wang, J., Zaron, E. D.: Global observations of fine-scale ocean surface topography with
the Surface Water and Ocean Topography (SWOT) Mission, *OceanObs2019, Frontiers in
Marine Science*, <https://doi.org/10.3389/fmars.2019.00232>, 2019.
- Munk, W.H., and Wunsch, C.: Abyssal recipes II: energetics of tidal and wind mixing, *Deep Sea
Res. I*, 45, 1977–2010. [http://dx.doi.org/10.1016/S0967-0637\(98\)00070-3](http://dx.doi.org/10.1016/S0967-0637(98)00070-3), 1998.
- Nagai, T., and Hibiya, T.: Internal tides and associated vertical mixing in the Indonesian
Archipelago, *J. Geophys. Res.-Oceans*, 120, 3373–3390, doi:10.1002/2014JC010592, 2015.
- Nash J.D., Kunze, E., Lee, C. M., and Sanford, T. B.: Structure of the baroclinic tide generated at
Kaena Ridge, Hawaii. *J. Phys. Oceanogr.*, 36, 1123–1135, 2006.
- Niwa, Y., and Hibiya, T.: Numerical study of the spatial distribution of the M2 internal tide in the
Pacific Ocean, *J. Geophys. Res.*, 106, 22,441–22,449, 2001.
- Niwa, Y., and Hibiya, T.: Three-dimensional numerical simulation of M2 internal tides in the East
China Sea, *J. Geophys. Res.*, 109, C04027, <https://doi.org/10.1029/2003JC001923>, 2004.
- Niwa, Y., and Hibiya, T.: Estimation of baroclinic tide energy available for deep ocean mixing
based on three-dimensional global numerical simulations, *J. Oceanogr.* 67, 493–502.
<https://doi.org/10.1007/s10872-011-0052-1>, 2011.
- Niwa, Y., and Hibiya, T.: Generation of baroclinic tide energy in a global three-dimensional
numerical model with different spatial grid resolutions, *Ocean Modelling*, 80, 59-73,
<https://doi.org/10.1016/j.ocemod.2014.05.003>, 2014.
- Nugroho, D., Koch-Larrouy, A., Gaspar, P., Lyard, F., Reffray, G., and Tranchant, B.: Modelling
explicit tides in the Indonesian seas: An important process for surface sea water
properties, *Mar. Poll. Bull.* 131(b), 7 – 18, 2017.
- Qin, X., Menviel, L., Sen Gupta, A., and van Sebille, E.: Iron sources and pathways into the Pacific
Equatorial Undercurrent, *Geophys. Res. Lett.*, 43, <https://doi.org/10.1002/2016GL070501>,
2016.
- Pinkel, R., Merrifield, M., Mc Phaden, M., Picaut J., Rutledge, S., Siegel, S., and Washburn L.:
Solitary waves in the western equatorial Pacific Ocean, *Geophys. Res. Lett.*, 24, 1603-1606,
1997.
- Ponte, A. L., and Klein, P.: Incoherent signature of internal tides on sea level in idealized
numerical simulations, *Geophys. Res. Lett.*, 42, 1520-1526, doi:10.1002/2014GL062583,
2015.

- 57 Price, J.F., and Yang, J.: Marginal Sea Overflows for Climate Simulations and Parameterizations,
58 E.P. Chassignet and J. Verron (Eds.), Kluwer Academic Publishers, 155-170, 1998.
- 59 Ray, R. D., and Mitchum, G. T.: Surface manifestation of internal tides in the deep ocean:
60 Observations from altimetry and island gauges, *Progress in Oceanography*, 40(1), 135-
61 162, 1997.
- 62 Ray, R. D., and Zaron, E.: M2 internal tides and their observed wavenumber spectra from satellite
63 altimetry, *J. Phys. Oceanogr.*, 46(1), 3–22, <https://doi.org/10.1175/JPO-D-15-0065.1>, 2016.
- 64 Robertson, R., and Field, A.: Baroclinic tides in the Indonesian Seas: Tidal fields and
65 comparisons to observations, *J. Geophys. Res.*, 113, C07031, doi:10.1029/2007JC004677,
66 2008.
- 67 Qiu, B., and Chen, S.: Seasonal modulations in the Eddy field of the South Pacific Ocean, *J. Phys.*
68 *Oceanogr.*, 34, 1515–1527, 2004.
- 69 Qu, T., and Lindstrom, E. J.: Northward intrusion of Antarctic intermediate water in the western
70 Pacific, *J. Phys. Oceanogr.*, 34(9), 2104–2118, [https://doi.org/10.1175/1520-0485\(2004\)034<2104:NIOAIW>2.0.CO;2](https://doi.org/10.1175/1520-0485(2004)034<2104:NIOAIW>2.0.CO;2), 2004.
- 71 Rudnick, D. L., Johnston, T. M. S., and Sherman, J. T.: High-frequency internal waves near the
72 Luzon
73 Strait observed by underwater gliders, *J. Geophys. Res.-Oceans*, 118, 774–784,
74 <https://doi.org/10.1002/jgrc.20083>, 2013.
- 75 Savage, A. C., Arbic, B. K., Richman, J. G., Shriver, J. F., Alford, M. H., Buijsman, M. C., Farrar, J. T.,
76 Sharma, H., Voet, G., Walcraft, A. J., and Zmudis, L. : Frequency content of sea surface
77 height variability from internal gravity waves to mesoscale eddies, *J. Geophys. Res.-*
78 *Oceans*, 122, 2519– 2538, <https://doi.org/10.1002/2016JC012331>, 2017.
- 79 Shriver, J., Arbic, B., Richman, J., Ray, R., Metzger, E., Wallcraft, A., and Timko, P.: An evaluation
80 of the barotropic and internal tides in a high-resolution global ocean circulation mode. *J.*
81 *Geophys. Res.-Oceans* 117(C10), 2012.
- 82 Shriver, J., Richman, J., and Arbic, B.: How stationary are the internal tides in a high-resolution
83 global ocean circulation model ?, *J. Geophys. Res.-Oceans*, 119, 2769 - 2787, 2014.
- 84 Simmons, H., Jayne, S., St. Laurent, L., and Weaver, J.: Tidally driven mixing in a numerical model
85 of the ocean general circulation, *Ocean Mod.*, 6(3-4), 245 – 263, 2004.
- 86 Srinivasan, K., McWilliams, J.C., Renault, L., Hristova, H.G., Molemaker, J., and Kessler, W.S.:
87 Topographic and Mixed Layer Submesoscale Currents in the Near-Surface Southwestern
88 Tropical Pacific, *J. Phys. Oceanogr.*, 47, 1221-1242, <https://doi.org/10.1175/JPO-D-16-0216.1>, 2017.
- 89 Tchilibou, M. Dynamique méso-sous-mésoéchelle et marée interne dans le Pacifique tropical :
90 implications pour l'altimétrie et la mer des Salomon, *Océanographie*. Université Paul
91 Sabatier Toulouse III, Français. (NNT: 2018TOU30292), 2018.
- 92 Tchilibou, M., Gourdeau, L., Morrow, R., Serazin, G., Djath, B., and Lyard, F.: Spectral signatures
93 of the tropical Pacific dynamics from model and altimetry: a focus on the meso-
94 /submesoscale range, *Ocean Sci.*, 14, 1283-1301, [https://doi.org/10.5194/os-14-1283-](https://doi.org/10.5194/os-14-1283-2018)
95 [2018](https://doi.org/10.5194/os-14-1283-2018), 2018.
- 96 Treguier, A. M., Barnier, B., de Miranda, A. P., Molines, J. M., Grima, N., Imbard, M., Madec, G.,
97 Messenger, C., Reynaud, T., and Michel, S.: An eddy-permitting model of the Atlantic
98 circulation: Evaluating open boundary conditions, *J. Geophys. Res.*, 106, 22115–22129,
99 <https://doi.org/10.1029/2000JC000376>, 2001.
- 100 Tsuchiya, M., R. Lukas, R. Fine, E. Firing, and E. Lindstrom, 1989: Source waters of the Pacific
101 Equatorial Undercurrent. *Prog. Oceanogr.*, 23, 101–147. Wunsch 1975.
- 102 Zaron, E. D.: Mapping the nonstationary internal tide with satellite altimetry, *J. Geophys. Res.-*
103 *Oceans*, 122, 539–554, <https://doi.org/10.1002/2016JC012487>, 2017.
- 104 Zhao, Z., Alford, M. H., MacKinnon, J. A., and Pinkel, R.: Long-range propagation of the
105 semidiurnal internal tide from the Hawaiian Ridge. *J. Phys. Oceanogr.*, 40, 713–736,
106 <https://doi.org/10.1175/2009JPO4207.1>, 2010.

- 09 Zhao, Z., Alford, M. H., Girton, J. B., Rainville, L., and Simmons, H. L.: Global observations of open-
10 ocean mode-1 M2 internal tides. *J. Phys. Oceanogr.*, 46, 1657–1684.
11 <https://doi.org/10.1175/JPO-D-15-0105.1>, 2016.
- 12 Zhao, Z.: The global mode-2 M2 internal tide. *J. Geophys. Res.-Oceans*, 123, 7725–7746.
13 <https://doi.org/10.1029/2018JC014475>, 2018.
- 14 Zilberman, N. V., Merrifield, M.A., Carter, G.S., Luther, D.S., Levine, M.D., and Boyd, T.J., 2011:
15 Incoherent nature of M2 internal tides at the Hawaiian Ridge. *J. Phys. Oceanogr.*, 41, 2021-
16 2036.
17
18

	$\nabla \cdot F_{bt}$		D_{bt}		C		$\nabla \cdot F_{bc}$		D_{bc}		P1 %		P2 %	
	Niño	Niña	Niño	Niña	Niño	Niña	Niño	Niña	Niño	Niña	Niño	Niña	Niño	Niña
Sol str	3.	2.93	-0.84	-0.86	-2.16	-2.07	0.53	0.7	-1.63	-1.37	72	71	75	66
Sol sud	6.83	5.89	-2.53	-2.11	-4.3	-3.78	1.27	0.75	-3.03	-3.03	63	64	70	80
PNG	1.75	1.81	-0.38	-0.45	-1.37	-1.36	0.76	0.73	-0.64	-0.63	79	75	47	46

Table 1: $\nabla \cdot F_{bt}$ ($\nabla \cdot F_{bc}$) is the divergence of the barotropic (baroclinic) flux, D_{bt} (D_{bc}) is the dissipation of the barotropic (baroclinic) flux, C is the conversion rate from barotropic to baroclinic energy. Units are in GW. P1 is the percentage of the barotropic energy converted into baroclinic energy and P2 is the percentage of the baroclinic energy dissipated within the box.

Figure captions

Figure 1: Bathymetry of the Solomon Sea over the domain of the regional simulation (in color, unit in m). The 50 m depth has a black contour. PNG: Papua New Guinea, NB: New Britain, NI: New Ireland, Vit. Str.: Vitiaz strait, Sol. Str.: Solomon Strait, Wdl arch.: Woodlark Archipelago. The arrows illustrate the different currents mentioned in the text (Dashed arrows are for surface currents, line arrows are for the thermocline currents). NGCC: New Guinea Coastal Current, NGCU: New Guinea Coastal UnderCurrent, SSI: Solomon Strait Inflow, EUC: Equatorial UnderCurrent, SEC: South Equatorial Current, NVJ: North Vanuatu Jet, GPC: Gulf of Papua Current. The bathymetric file is the NOAA/ETOPO2v2 bathymetric file from the Smith & Sandwell database (doi: 10.7289/V5J1012Q).

Figure 2: Mean surface EKE (shading, unit: $\text{cm}^2 \text{s}^{-2}$) and mean surface circulation (arrows) from the 3-month TIDE simulations during a) the El Niño state and b) the La Niña state. Note the change of colorbar between the two ENSO states. White color is for bathymetry less than 50 m depth. Isobathymetric lines are from the NOAA/ETOPO2v2 bathymetric file from the Smith & Sandwell database (doi: 10.7289/V5J1012Q).

Figure 3: Root-mean-square of SSH variability for the 3-month periods of the El Niño state (left column) and of the La Niña state (right column). Unit is in cm. The top panel is the full SSH variance (a, b), the second panel is the mesoscale variability (periods > 48h) (c, d), the third panel is the high frequency variability (periods < 48h) (e, f), dominated by the internal tides (both coherent and incoherent components) and the bottom panel is the incoherent internal tide variability (g, h). Note the change of colorbar for the full and mesoscale variability of the La Niña period. Isobathymetric lines are from the NOAA/ETOPO2v2 bathymetric file from the Smith & Sandwell database (doi: 10.7289/V5J1012Q). White color is for bathymetry less than 50 m depth.

Figure 4: Latitude/depth section at 154°E of mean salinity from a) the R36Td simulation, b) CARS climatology, and of salinity anomalies for the 3 month c) El Niño period and d) La Niña period, relative to the full R36Td period. The Solomon Sea section is between the topographic features (vertical black lines) at 12°S and 6°S. The black contours highlight the upper thermocline layer (UTW).

Figure 5: Mean N profile averaged for the Solomon Sea section at 154°E from CARS climatology (black), and from the R36Td TIDES simulation averaged over the entire 3-year period (blue), the 3-month El Niño period (green) and the 3-month La Niña period (red). The yellow line is for the R36d NOTIDES simulation averaged over the entire 3-year period. Unit is in s^{-1} .

Figure 6: a) SSH frequency spectra averaged over the Solomon Sea area based on the 3 month hourly outputs of the El Niño period for the R36h simulation (No tides, in yellow), for the R36Th simulation including barotropic and baroclinic tides (Tides, in blue), baroclinic tides only (Tides-BT, in pink), incoherent baroclinic tides only (Tides-BT-BC, in cyan). b) Zoom on SSH frequency spectra showing the diurnal, semidiurnal, and quart diurnal signature of baroclinic tides calculated during the El Niño period (in green) and the La Niña period (in red). For clarity the green spectrum is shifted by 2 hours.

Figure 7: SSH M2 barotropic tide from a) FES2014, and b) the R36Th simulation. Amplitude is in color (unit in cm) and the contours are phase lines. Isobathymetric lines are from the NOAA/ETOPO bathymetric file from the Smith & Sandwell database (doi: 10.7289/V5J1012Q). White color is for bathymetry less than 50 m depth.

3 Figure 8: SSH amplitude of the stationary M2 baroclinic tide as estimated from a) altimetry by Ray
) and Zaron (2016), the R36Th simulations during the 3-months of b) the El Niño period, and c) the
) La Niña period. Unit in cm. Isobathymetric lines are from the NOAA/ETOPO2v2 bathymetric file from
1 the Smith & Sandwell database (doi: 10.7289/V5J1012Q). White color is for bathymetry less than
2 50 m depth.
3

4 Figure 9: Conversion rate (C , top), the baroclinic flux divergence ($\nabla \cdot \mathbf{F}$, middle), and the dissipation
5 rate (D , bottom) for the M2 harmonic (negative values shaded in blue, positive values in red,
6 unit: Wm^{-2}). The corresponding barotropic and baroclinic energy flux are superimposed with
7 arrows in the top and middle panels, with a scaling of 100 kW m^{-1} and 2 kW m^{-1} , respectively. The
8 left column corresponds to the El Niño period and the right column to the La Niña period. The
9 boxes define the different generation areas where energetics are quantified in Table 1.
) Isobathymetric lines are from the NOAA/ETOPO2v2 bathymetric file from the Smith & Sandwell
1 database (doi: 10.7289/V5J1012Q). White color is for bathymetry less than 50 m depth.
2

3 Figure 10: Modal decomposition of the M2 energy flux during the 3-month El Niño (top) and La
4 Niña (bottom) periods, corresponding to mode 1 (left), and mode 2 (right). Mode 1 flux is scaled
5 with arrows of 2 kW m^{-1} and mode 2 flux with arrows of 500 W m^{-1} . The shading is the amplitude
6 (unit in Wm^{-1}). Isobathymetric lines are from the NOAA/ETOPO2v2 bathymetric file from the
7 Smith & Sandwell database (doi: 10.7289/V5J1012Q). White color is for bathymetry less than 50
8 m depth.
9

) Figure 11: Vertical section at 154°E of the mean meridional energy flux estimated during a) El
1 Niño state and b) La Niña state (unit in W m^{-2}). The corresponding isopycnals are in contours;
2 with $\sigma = 23.5 \text{ kg m}^{-3}$ and $\sigma = 24.5 \text{ kg m}^{-3}$ in bold.
3

4 Figure 12: Mean salinity distribution (in color) and mean circulation (arrows) of the UTW waters
5 from the 3-year a) NOTIDE simulation, b) TIDE simulation, and c) the multi-decadal CARS
6 climatology. Isobathymetric lines are from the NOAA/ETOPO2v2 bathymetric file from the Smith
7 & Sandwell database (doi: 10.7289/V5J1012Q). White color is for bathymetry less than 50 m
8 depth.
9

) Figure 13: Mean difference in temperature (left, unit in $^\circ\text{C}$) and salinity (right) between the
1 simulation with tides and the simulation without tides (TIDES-NOTIDES) for the surface waters
2 (SW, top), the upper thermocline waters (UTW, middle), and the intermediate waters (IW,
3 bottom). The density range for these water masses are defined in the text. Isobathymetric lines
4 are from the NOAA/ETOPO2v2 bathymetric file from the Smith & Sandwell database (doi:
5 10.7289/V5J1012Q). White color is for bathymetry less than 50 m depth.
6

7 Figure 14: TIDE – NOTIDE Temperature anomalies (in color, $^\circ\text{C}$) and mean circulation (arrows) for
8 the SW waters during (a) the El Niño period and (b) the La Niña period. Isobathymetric lines are
9 from the NOAA/ETOPO2v2 bathymetric file from the Smith & Sandwell database (doi:
) 10.7289/V5J1012Q). White color is for bathymetry less than 50 m depth.
1
2

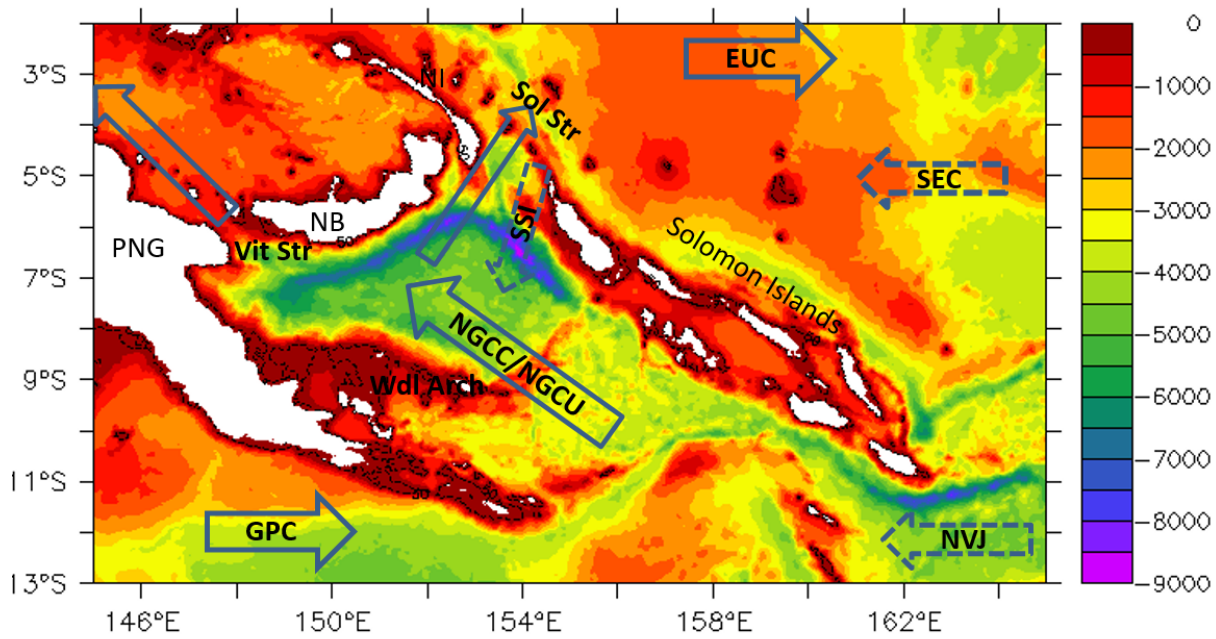


Figure 1: Bathymetry of the Solomon Sea over the domain of the regional simulation (in color, unit in m). The 50 m depth has a black contour. PNG: Papua New Guinea, NB: New Britain, NI: New Ireland, Vit. Str.: Vitiāz strait, Sol. Str.: Solomon Strait, Wdl arch.: Woodlark Archipelago. The arrows illustrate the different currents mentioned in the text (Dashed arrows are for surface currents, line arrows are for the thermocline currents). NGCC: New Guinea Coastal Current, NGCU: New Guinea Coastal UnderCurrent, SSI: Solomon Strait Inflow, EUC: Equatorial UnderCurrent, SEC: South Equatorial Current, NVJ: North Vanuatu Jet, GPC: Gulf of Papua Current. The bathymetric file is the NOAA/ETOPO2v2 bathymetric file from the Smith & Sandwell database (doi: 10.7289/V5J1012Q).

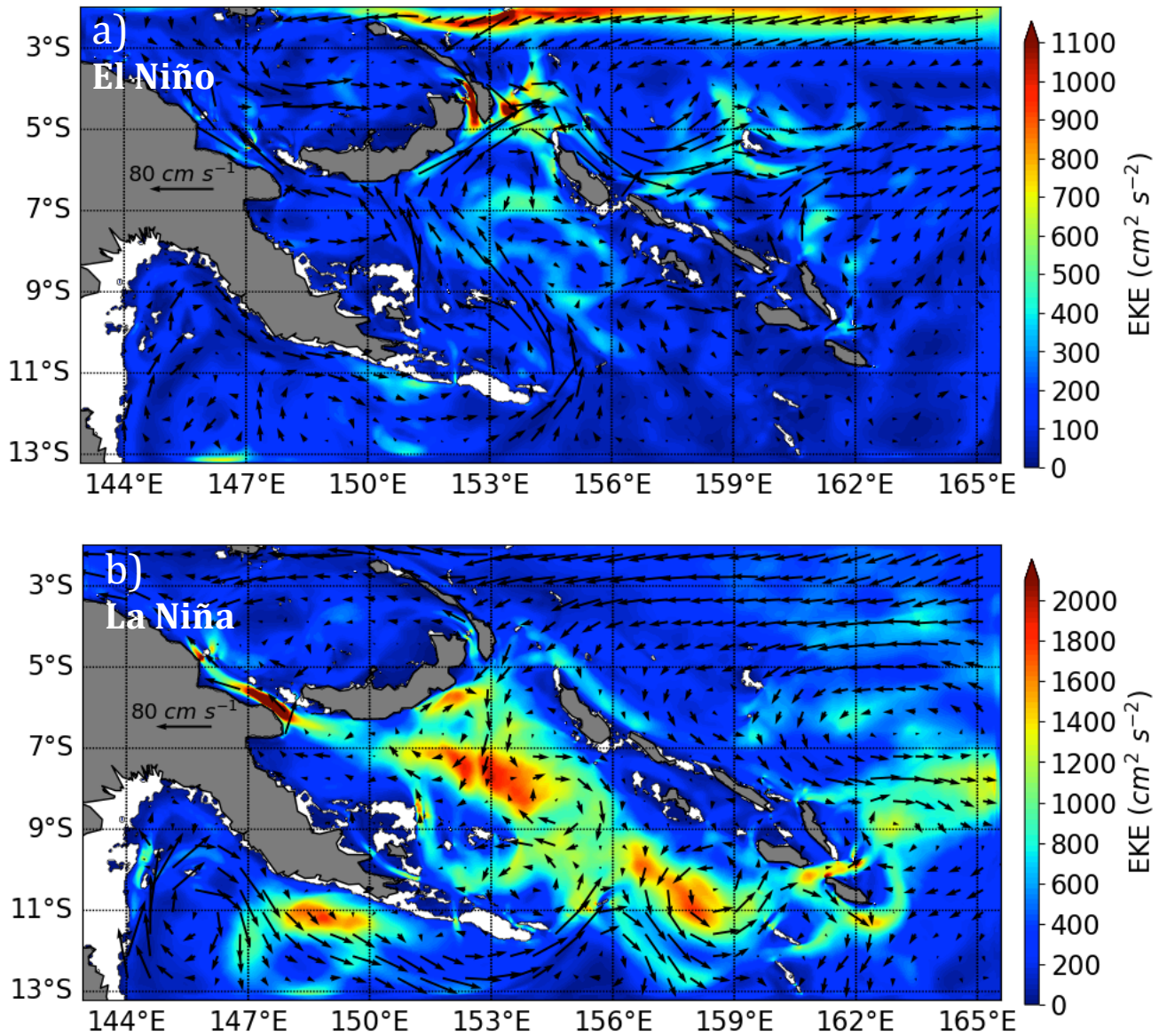
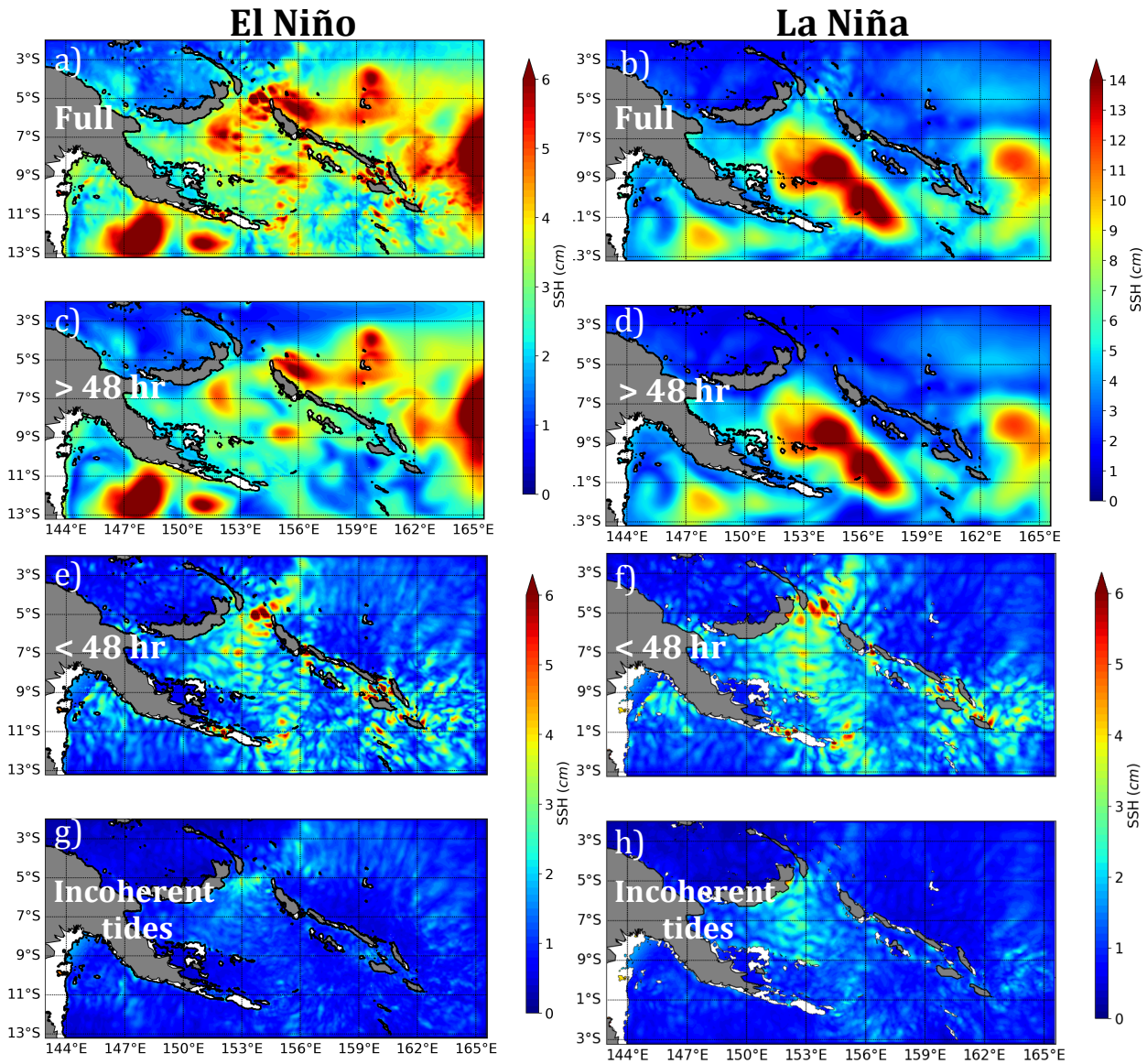


Figure 2: Mean surface EKE (shading, unit: $\text{cm}^2 \text{s}^{-2}$) and mean surface circulation (arrows) from the 3-month TIDE simulations during a) the El Niño state and b) the La Niña state. Note the change of colorbar between the two ENSO states. White color is for bathymetry less than 50 m depth. Isobathymetric lines are from the NOAA/ETOPO2v2 bathymetric file from the Smith & Sandwell database (doi: 10.7289/V5J1012Q).



5
 6
 7 Figure 3: Root-mean-square of SSH variability for the 3-month periods of the El Niño state (left column) and of the La Niña state (right column). Unit is in cm. The top panel is the full SSH variance (a, b), the second panel is the mesoscale variability (periods > 48h) (c, d), the third panel is the high frequency variability (periods < 48h) (e, f), dominated by the internal tides (both coherent and incoherent components) and the bottom panel is the incoherent internal tide variability (g, h). Note the change of colorbar for the full and mesoscale variability of the La Niña period. Isobathymetric lines are from the NOAA/ETOPO2v2 bathymetric file from the Smith & Sandwell database (doi: 10.7289/V5J1012Q). White color is for bathymetry less than 50 m depth.

5
 6

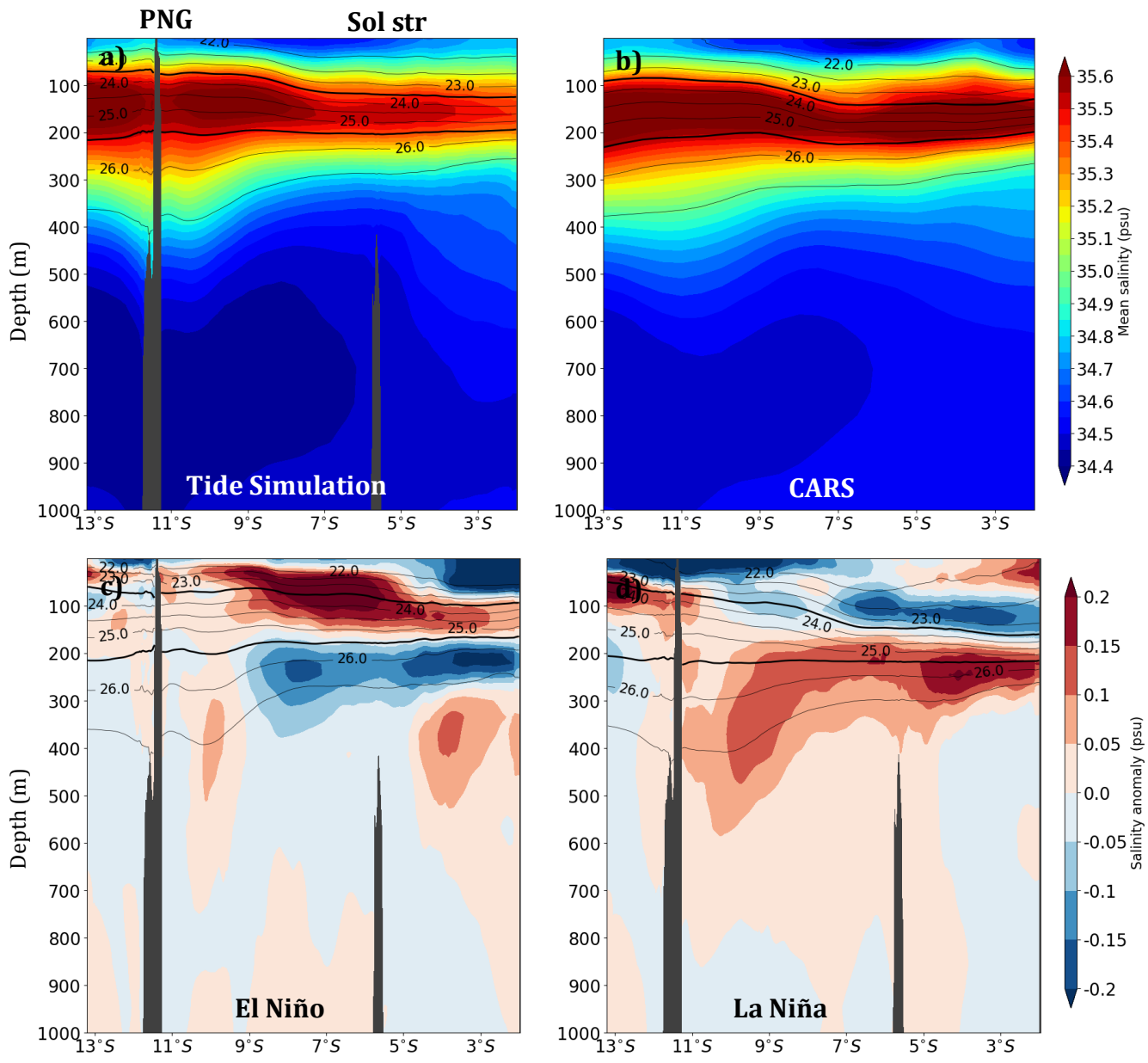


Figure 4: Latitude/depth section at 154°E of mean salinity from a) the R36Td simulation, b) CARS climatology, and of salinity anomalies for the 3 month c) El Niño period and d) La Niña period, relative to the full R36Td period. The Solomon Sea section is between the topographic features (vertical black lines) at 12°S and 6°S. The black contours highlight the upper thermocline layer (UTW).

3
)
)
 l
 2
 }
 4

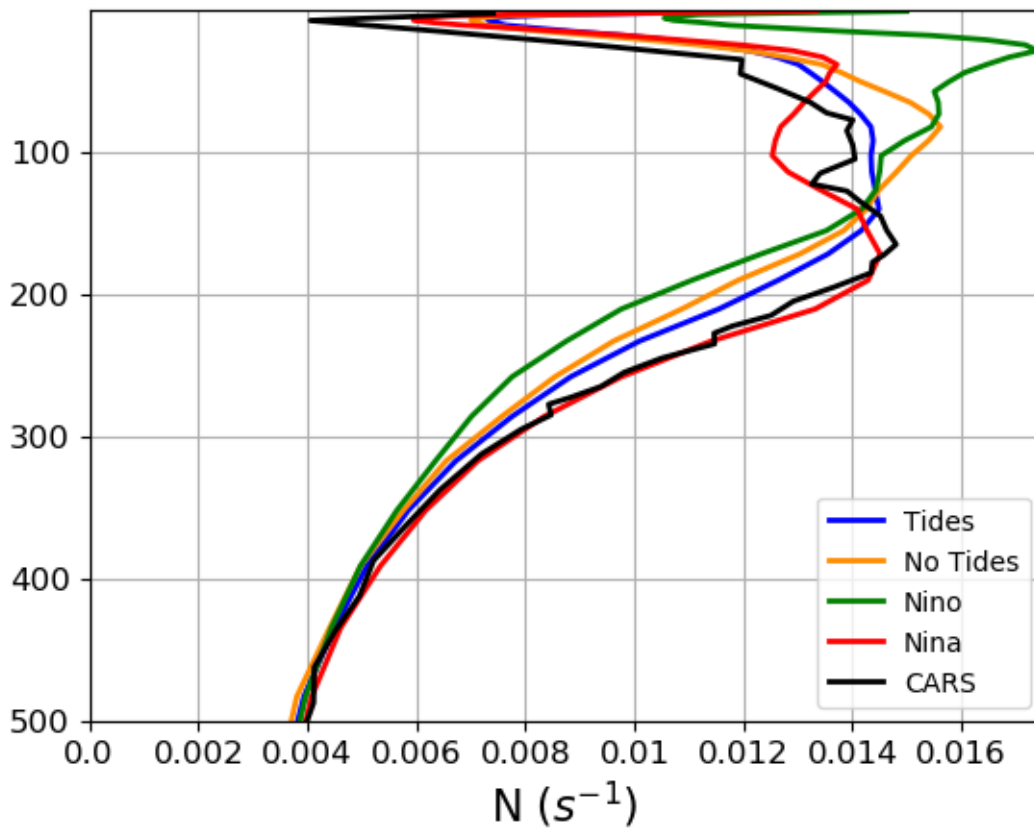


Figure 5: Mean N profile averaged for the Solomon Sea section at 154°E from CARS climatology (black), and from the R36Td TIDES simulation averaged over the entire 3-year period (blue), the 3-month El Niño period (green) and the 3-month La Niña period (red). The yellow line is for the R36d NOTIDES simulation averaged over the entire 3-year period. Unit is in s^{-1} .

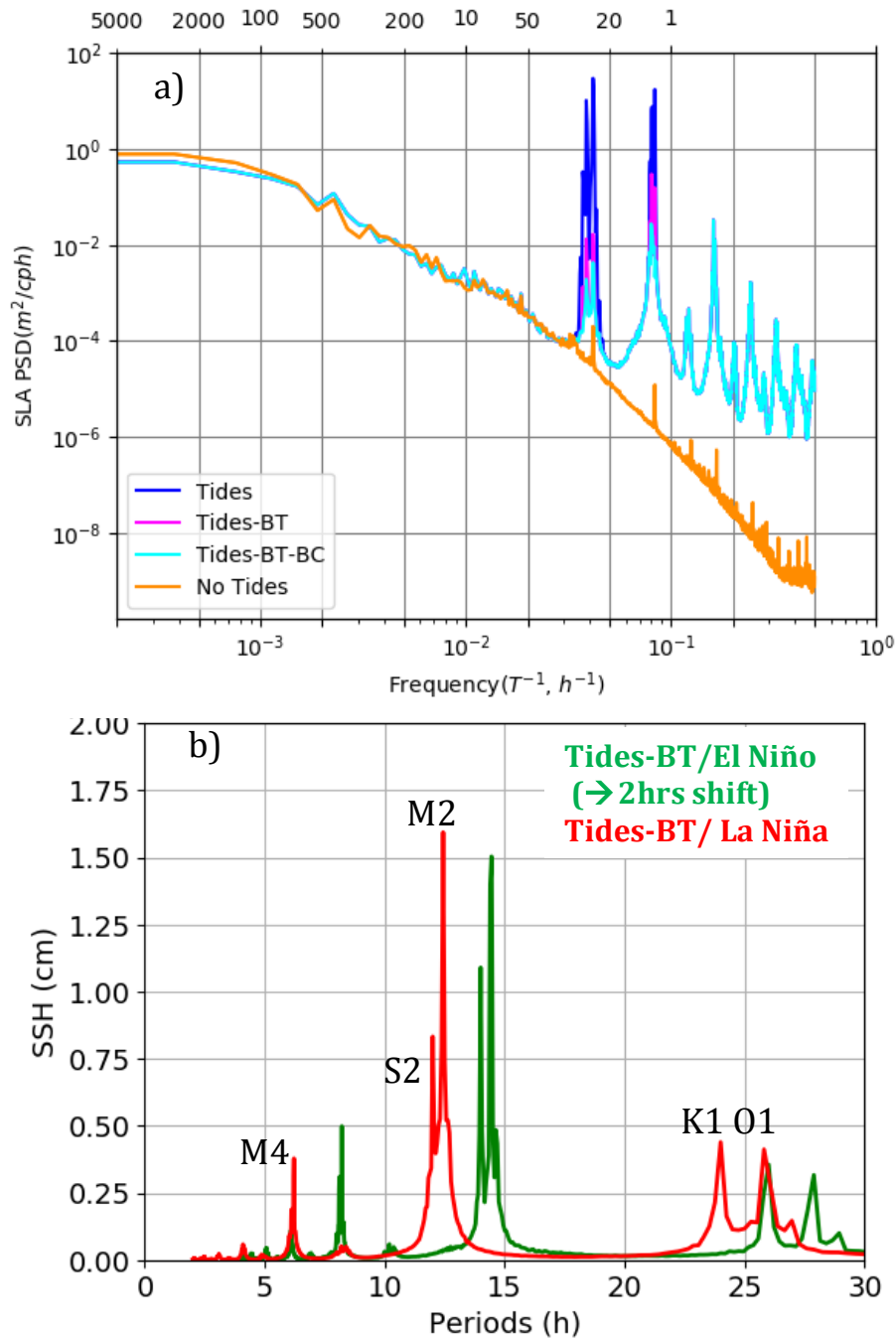


Figure 6: a) SSH frequency spectra averaged over the Solomon Sea area based on the 3 month hourly outputs of the El Niño period for the R36h simulation (No tides, in yellow), for the R36Th simulation including barotropic and baroclinic tides (Tides, in blue), baroclinic tides only (Tides-BT, in pink), incoherent baroclinic tides only (Tides-BT-BC, in cyan). b) Zoom on SSH frequency spectra showing the diurnal, semidiurnal, and quart diurnal signature of baroclinic tides calculated during the El Niño period (in green) and the La Niña period (in red). For clarity the green spectrum is shifted by 2 hours.

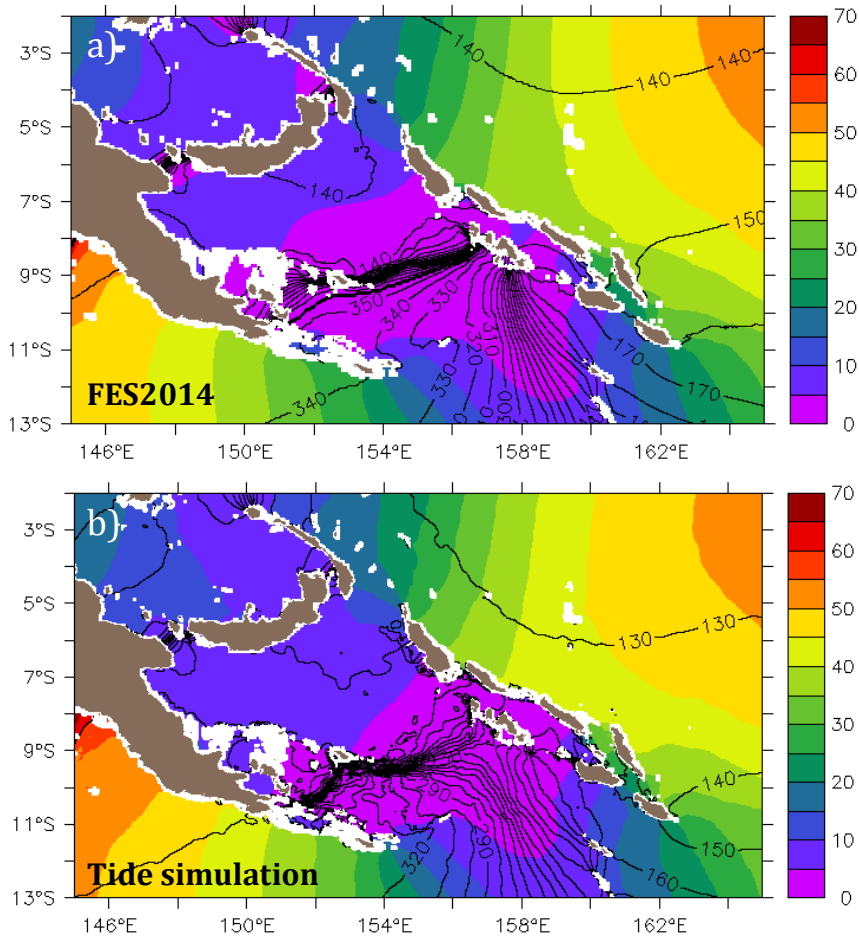


Figure 7: SSH M2 barotropic tide from a) FES2014, and b) the R36Th simulation. Amplitude is in color (unit in cm) and the contours are phase lines. Isobathymetric lines are from the NOAA/ETOPO bathymetric file from the Smith & Sandwell database (doi: 10.7289/V5J1012Q). White color is for bathymetry less than 50 m depth.

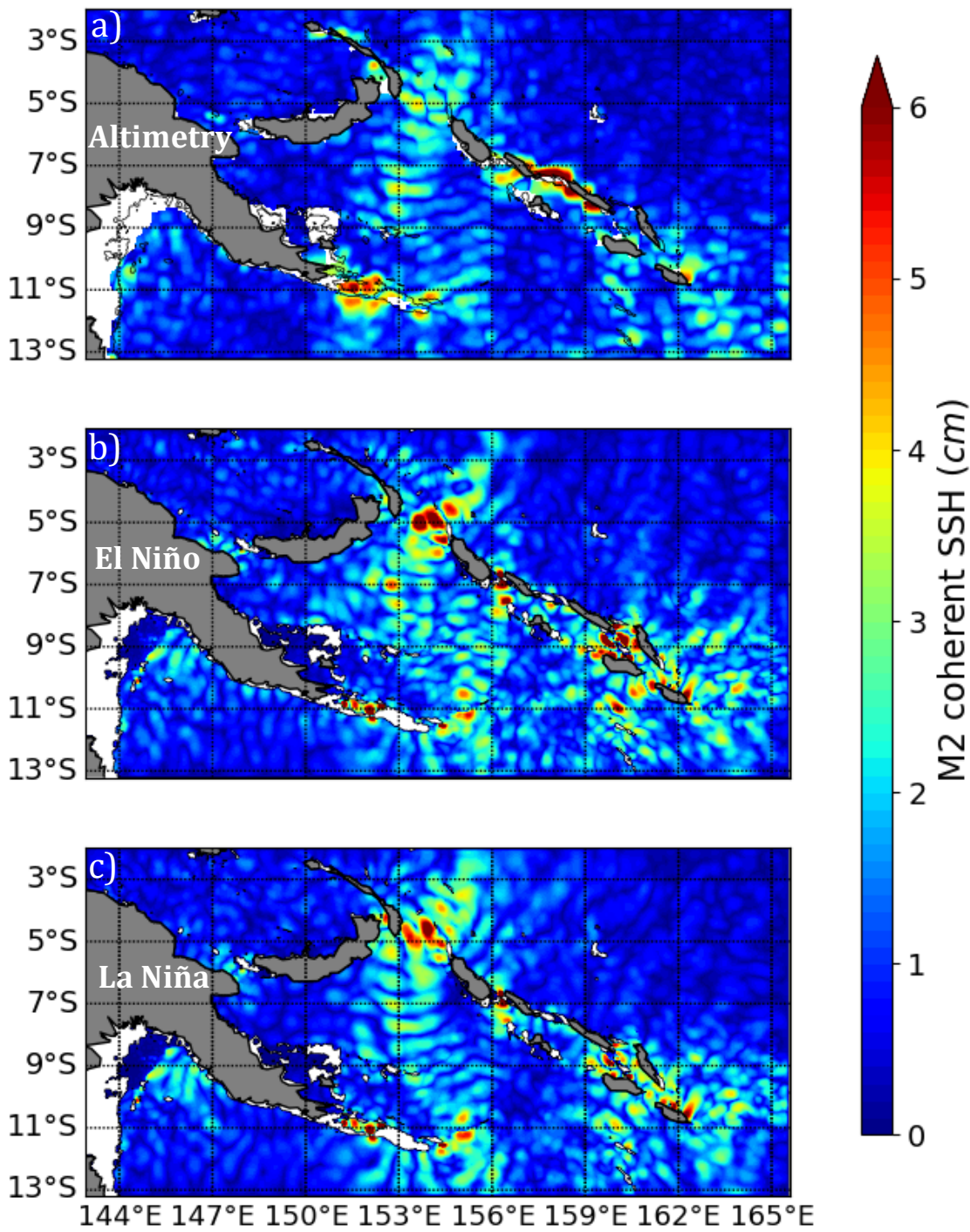


Figure 8: SSH amplitude of the stationary M2 baroclinic tide as estimated from a) altimetry by Ray and Zaron (2016), the R36Th simulations during the 3-months of b) the El Niño period, and c) the La Niña period. Unit in cm. Isobathymetric lines are from the NOAA/ETOPO2v2 bathymetric file from the Smith & Sandwell database (doi: 10.7289/V5J1012Q). White color is for bathymetry less than 50 m depth.

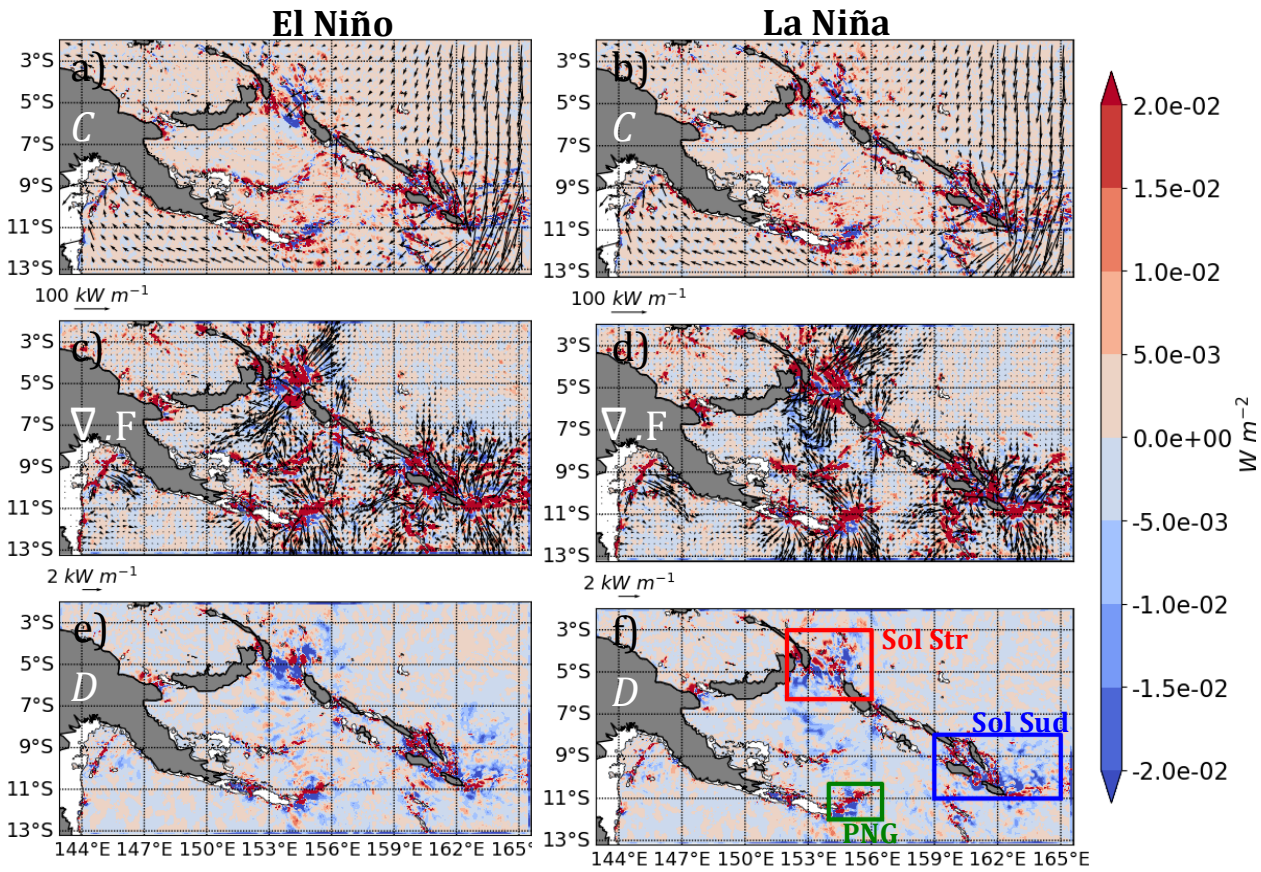


Figure 9: Conversion rate (C, top), the baroclinic flux divergence ($\nabla \cdot \mathbf{F}$, middle), and the dissipation rate (D, bottom) for the M2 harmonic (negative values shaded in blue, positive values in red, unit: W m^{-2}). The corresponding barotropic and baroclinic energy flux are superimposed with arrows in the top and middle panels, with a scaling of 100 kW m^{-1} and 2 kW m^{-1} , respectively. The left column corresponds to the El Niño period and the right column to the La Niña period. The boxes define the different generation areas where energetics are quantified in Table 1. Isobathymetric lines are from the NOAA/ETOPO2v2 bathymetric file from the Smith & Sandwell database (doi: 10.7289/V5J1012Q). White color is for bathymetry less than 50 m depth.

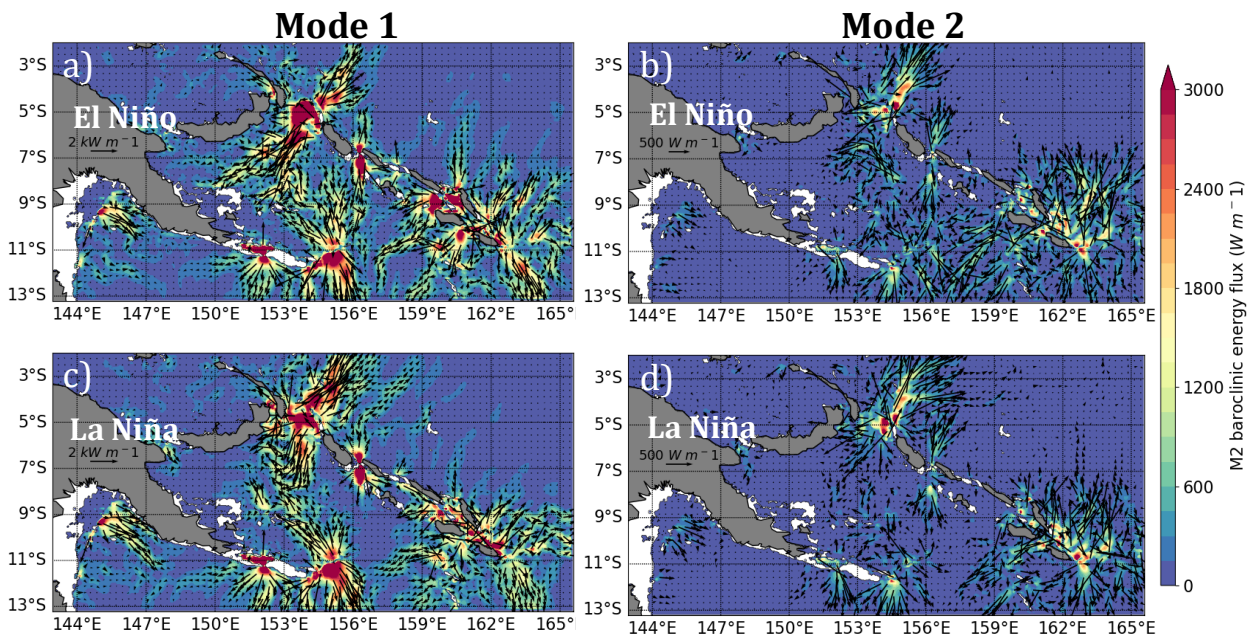


Figure 10: Modal decomposition of the M2 energy flux during the 3-month El Niño (top) and La Niña (bottom) periods, corresponding to mode 1 (left), and mode 2 (right). Mode 1 flux is scaled with arrows of $2 kW m^{-1}$ and mode 2 flux with arrows of $500 W m^{-1}$. The shading is the amplitude (unit in $W m^{-1}$). Isobathymetric lines are from the NOAA/ETOPO2v2 bathymetric file from the Smith & Sandwell database (doi: 10.7289/V5J1012Q). White color is for bathymetry less than 50 m depth.

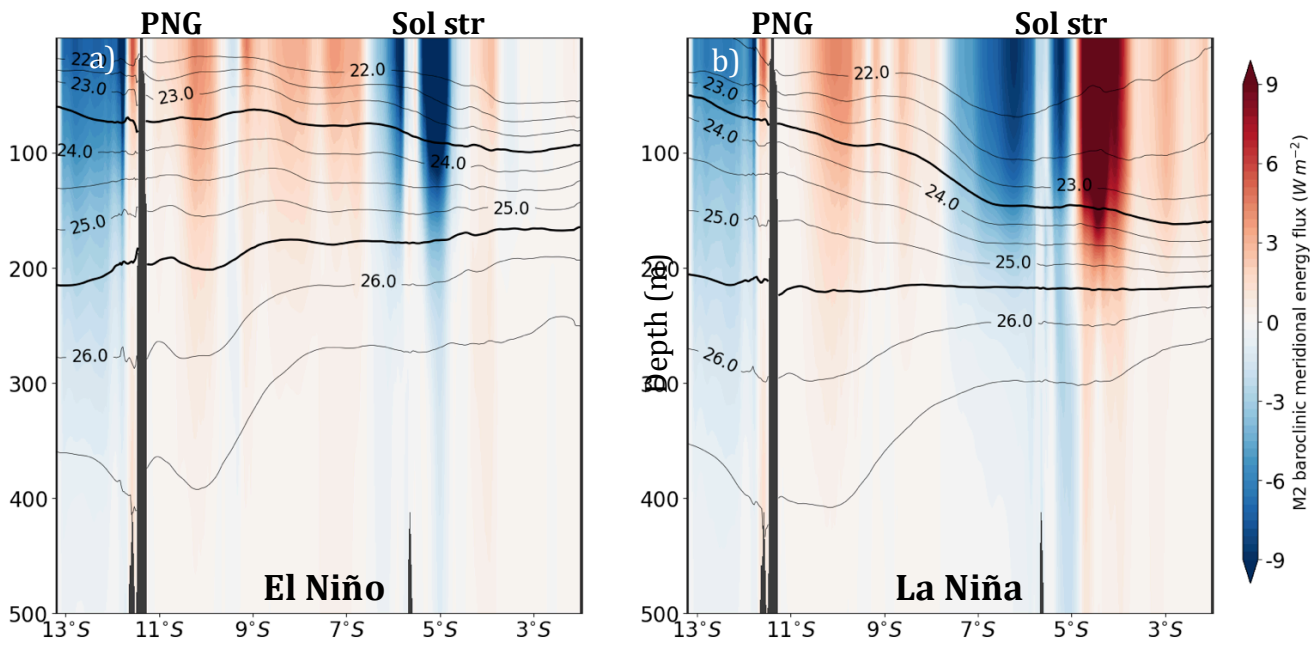


Figure 11: Vertical section at 154°E of the mean meridional energy flux estimated during a) El Niño state and b) La Niña state (unit in $W m^{-2}$). The corresponding isopycnals are in contours; with $\sigma = 23.5 kg m^{-3}$ and $\sigma = 24.5 kg m^{-3}$ in bold.

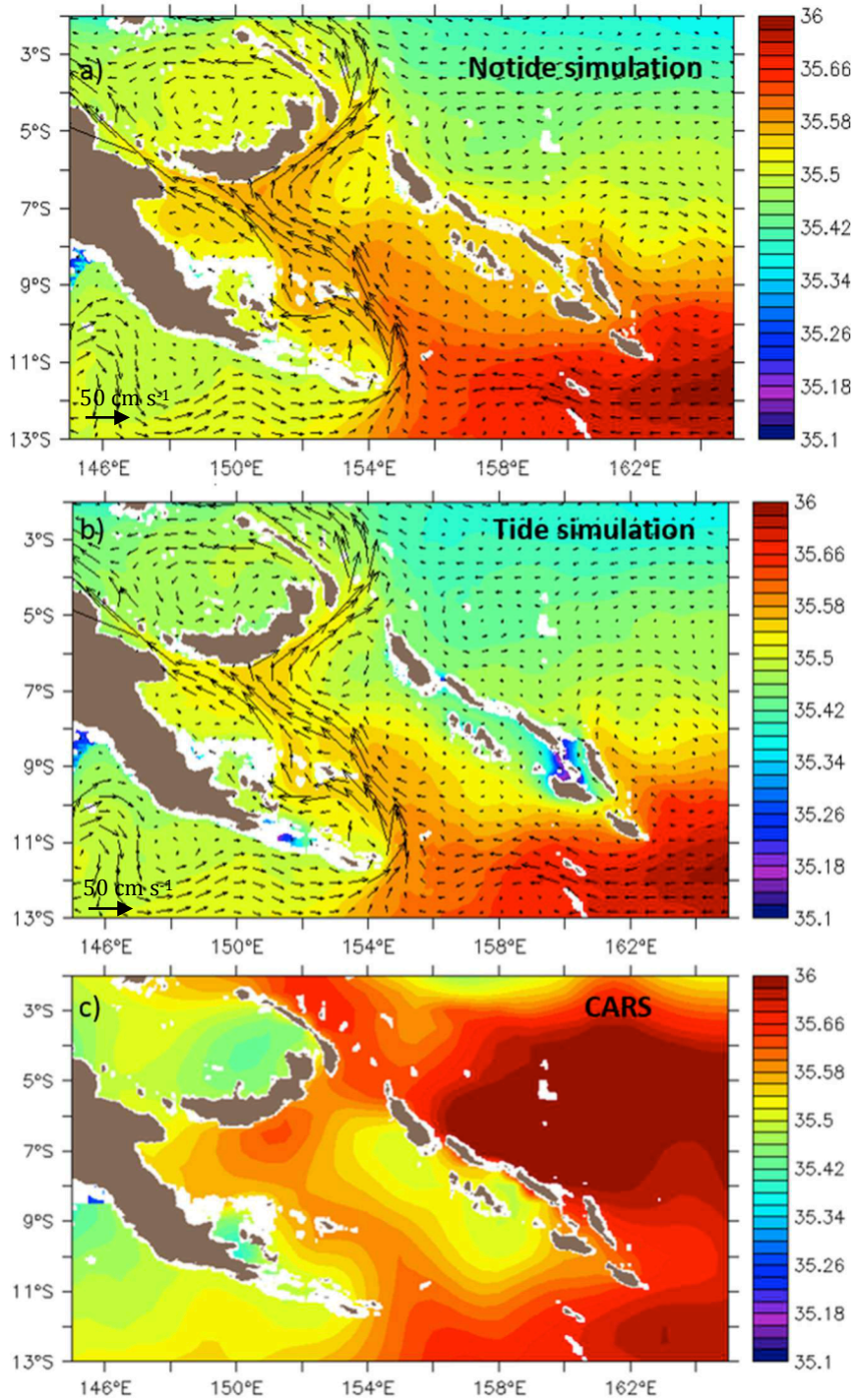


Figure 12: Mean salinity distribution (in color) and mean circulation (arrows) of the UTW waters from the 3-year a) NOTIDE simulation, b) TIDE simulation, and c) the multi-decadal CARS climatology. Isobathymetric lines are from the NOAA/ETOPO2v2 bathymetric file from the Smith & Sandwell database (doi: 10.7289/V5J1012Q). White color is for bathymetry less than 50 m depth.

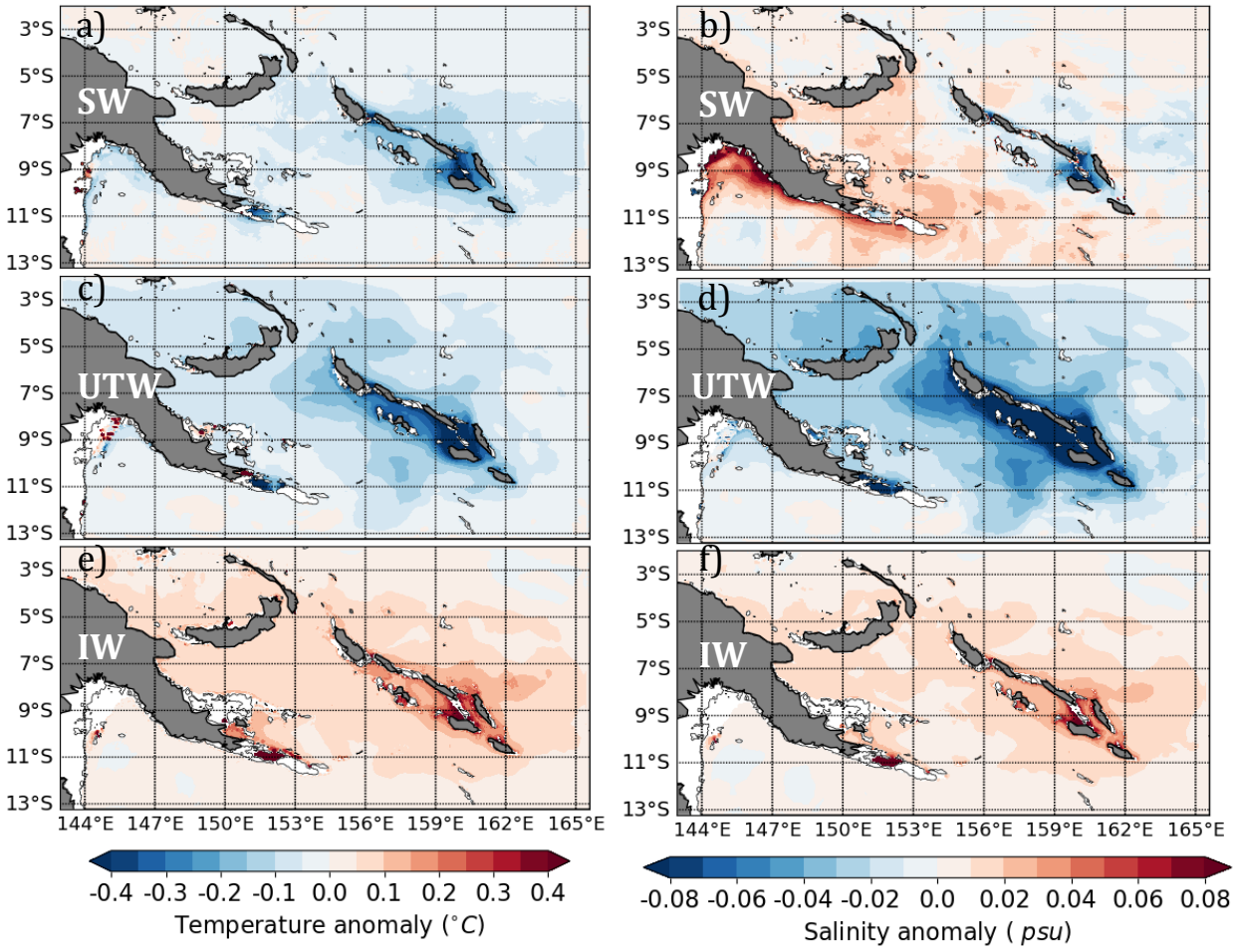


Figure 13: Mean difference in temperature (left, unit in °C) and salinity (right) between the simulation with tides and the simulation without tides (TIDES-NOTIDES) for a, b) the surface waters (SW, top), c, d) the upper thermocline waters (UTW, middle), and e, f) the intermediate waters (IW, bottom). The density range for these water masses are defined in the text. Isobathymetric lines are from the NOAA/ETOPO2v2 bathymetric file from the Smith & Sandwell database (doi: 10.7289/V5J1012Q). White color is for bathymetry less than 50 m depth.

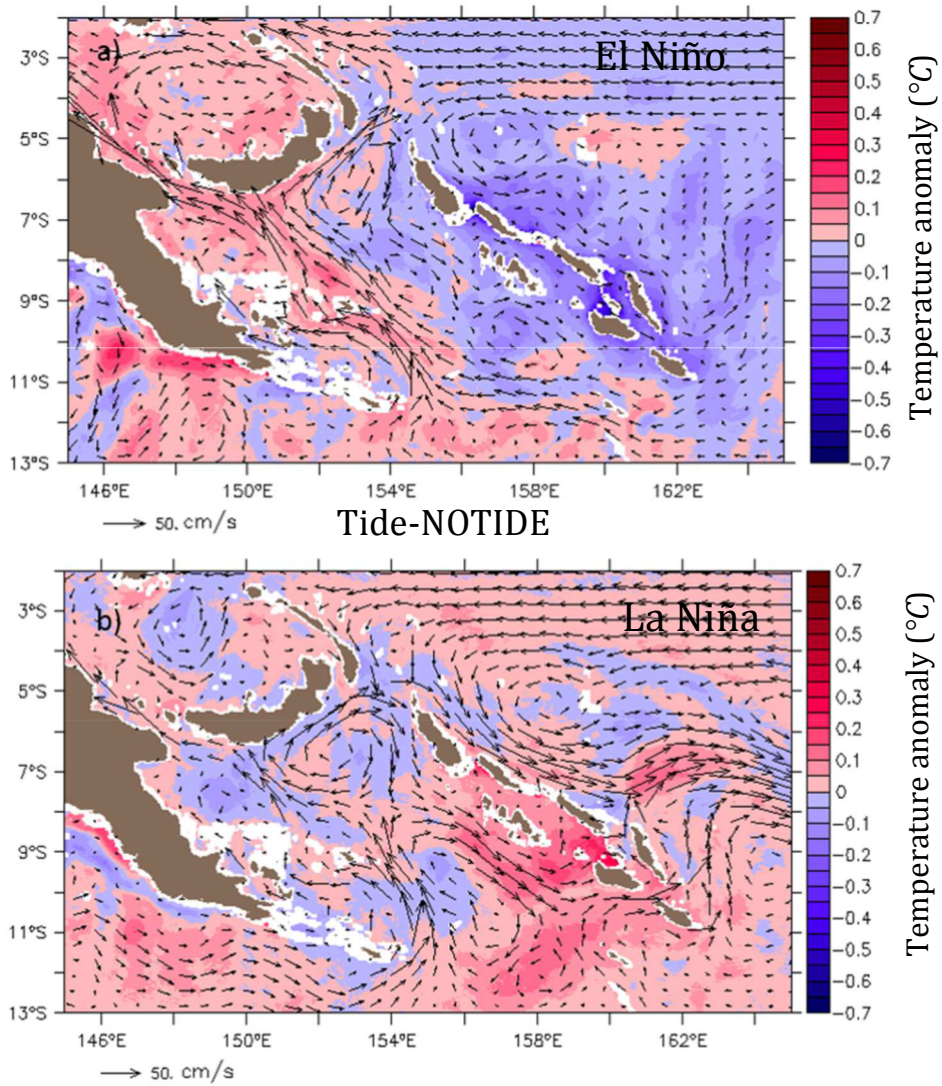


Figure 14: TIDE – NOTIDE Temperature anomalies (in color, °C) and mean circulation (arrows) for the SW waters during a) the El Niño period and b) the La Niña period. Isobathymetric lines are from the NOAA/ETOPO2v2 bathymetric file from the Smith & Sandwell database (doi: 10.7289/V5J1012Q). White color is for bathymetry less than 50 m depth.